QUANTIFYING THE EFFECT OF KEROGEN ON ELECTRICAL RESISTIVITY MEASUREMENTS IN ORGANIC-RICH SOURCE ROCKS

A Thesis

by

NIKHIL REDDY KETHIREDDY

Submitted to the Office of Graduate and Professional Studies of
Texas A&M University
in partial fulfillment of the requirements for the degree of

MASTER OF SCIENCE

Chair of Committee,	Zoya Heidari
Committee Members,	Walter B. Ayers
	Yalchin Efendiev
Head of Department,	Dan Hill

December 2013

Major Subject: Petroleum Engineering

ABSTRACT

Interpretation of electrical resistivity logs in organic-rich source rocks has been challenging for petrophysicists. Conventional resistivity-porosity-saturation models (e.g., Archie's, Dual-Water, and Waxman-Smits equations) assume that saline water is the only conductive part of the formation. However, this assumption is not reliable in organic-rich source rocks in the presence of highly mature organic matter, clay, and pyrite. Previous experimental studies indicate that aromaticity of kerogen increases with an increase in thermal maturity, which might lead to conductive behavior of kerogen. In this thesis, I investigated and quantified the effect of conductive kerogen on electrical resistivity of organic-rich source rocks.

First, I investigated the reliability of conventional resistivity-porosity-saturation models in the assessment of fluid saturations in organic-rich source rocks using well logs and core measurements in the Haynesville shale-gas formation. Next, I numerically simulated electric field, electric currents, and electrical resistivity of pore-scale images of organic-rich source rocks. I quantified the effect of (a) volumetric concentration of kerogen, (b) kerogen conductivity, and (c) spatial connectivity of kerogen-water network on electrical resistivity of rocks using pore-scale numerical simulations.

Well-log interpretation of the Haynesville shale-gas formation showed conventional resistivity-porosity-saturation models underestimate hydrocarbon saturation by 20% -

40% in the zones with high volumetric concentration of kerogen. In this thesis, I showed that the error in estimates of hydrocarbon saturation could be due to the impact of kerogen on electrical resistivity measurements. Pore-scale numerical simulations confirmed that conventional resistivity-porosity-saturation models could lead to 10% - 23% improvement in estimates of hydrocarbon saturation if the impact of conductive kerogen is taken into account. Results of this thesis act as the first step towards improving conventional resistivity-porosity-saturation models for estimation of fluid saturations in organic-rich source rocks.

DEDICATION

This thesis is dedicated to my parents for their unconditional love, endless support, and encouragement.

ACKNOWLEDGEMENTS

This thesis would not have been possible without the help, support and patience of my committee chair, Dr. Zoya Heidari, not to mention her advice and unsurpassed technical knowledge. I also want to thank the other members of my committee, Dr. Walter B. Ayers and Dr. Yalchin Efendiev as well as Dr. Michael C. Pope for their guidance and their time reviewing my thesis.

The work reported in this thesis was funded by the Crisman Institute of Petroleum Research at the Harold Vance Department of Petroleum Engineering and Texas A&M Multi-Scale Formation Evaluation Joint Industry Research Program, jointly sponsored by Anadarko, Baker Hughes, BG, BP, Chevron, ConocoPhillips, Devon Energy, Drilinginfo, ENI, ExxonMobil, Halliburton, Hess, IHS, Marathon, M-I SWACO, NETL, Nexen, Saudi Aramco, Schlumberger, Shell, SPE, TOTAL, and Woodside. My sincere gratitude goes to Society of Petroleum Engineers (SPE) for supporting this project via Junior Faculty Research Initiation Award. I thank the Texas A&M Supercomputing Facility for providing computing resources used for the numerical simulations in this thesis.

I would also like to thank my colleagues and friends in the Department of Petroleum Engineering. Thanks go to Huangye Chen, Mehrnoosh Saneifar, Alvaro Aranibar, and Lu Chi for their support throughout and in promoting a stimulating and welcoming

academic environment. The most special thanks goes to my partner and friend, Poojitha Valasareddy, for her love, kindness and support she has shown during the past two years. Finally, I would like to thank my parents and sister for their encouragement and support. Everything I am, I owe to them.

NOMENCLATURE

a	Archie's factor, [ ]
C_k	Volumetric concentration of kerogen, [%]
$C_{Plagioclase}$	Volumetric concentration of plagioclase, [%]
C_{Quartz}	Volumetric concentration of quartz, [%]
E	Electric field, [V/m]
m	Archie's porosity exponent, [ ]
n	Archie's saturation exponent, [ ]
J	Electric displacement field, [C/m^2]
R_{effK}	Resistivity of kerogen-gas system, [ohm-m]
R_k	Resistivity of kerogen, [ohm-m]
R_o	Vitrinite reflectance
S_g	Total water saturation, [%]
S_w	Total gas saturation, [%]
V	Electric potential, [V]
V_g	Volume of gas, [m^3]
V_{gk}	Total volume of gas-bearing kerogen, [m^3]
V_k	Volume of kerogen, [m^3]
V_t	Total volume of the domain, [m^3]
V_w	Volume of water, [m^3]
W_{TOC}	Weight concentration of TOC, [%]

Δt	Compressional slowness, [μs/ft]
ϕ_k	Kerogen porosity, [%]
ϕ_t	Total porosity, [%]
ρ_{grain}	Core grain density
σ	Electrical conductivity, [S/m]
2D	Two-dimensional
3D	Three-dimensional
CPU	Central Processing Unit
ECS	Elemental Capture Spectroscopy
FIB-SEM	Focused Ion Beam-Scanning Electron Microscopy
FT-IR	Fourier Transform-Infrared Spectroscopy
GR	Gamma Ray
LOM	Level Of Metamorphism
NMR	Nuclear Magnetic Resonance
PDE	Partial Differential Equation
PEF	Photo Electric Factor
QMR	Quasi-Minimal Residual
SEM	Scanning Electron Microscopy
TOC	Total Organic Carbon
XRD	X-Ray Diffraction

TABLE OF CONTENTS

Page

LIST OF FIGURES

Page

LIST OF TABLES

Page

CHAPTER I

INTRODUCTION AND LITERATURE REVIEW

This thesis quantifies the impact of volumetric concentration of kerogen, electrical resistivity of kerogen, kerogen porosity, salt concentration of connate water, and connectivity of kerogen-water network on electrical resistivity measurements in organic-rich source rocks. First, this thesis investigates the reliability of conventional resistivity-porosity-saturation models in the assessment of fluid saturations in organic-rich source rocks using well logs and core measurements from the Haynesville shale-gas formation. Second, a numerical modeling method is introduced for simulating electric field potential, electric currents, and electrical resistivity of pore-scale rock images in organic-rich source rocks. Finally, pore-scale numerical simulations are used to quantify the effect of (a) volumetric concentration of kerogen, (b) kerogen conductivity, and (c) connectivity of kerogen-water network on electrical resistivity of organic-rich source rocks.

1.1 Background

Petrophysical and compositional evaluation of organic-rich source rocks remains a major technical challenge for the petroleum industry, because of complex pore structure and lithology as well as the lack of protocols for core measurements in these unconventional reservoirs (Ramirez et al., 2011). Conventional well-log interpretation techniques are

usually calibrated using core data and applied to unconventional reservoirs. Recent studies (Passey et al., 2010; Sondergeld et al., 2010) describe significant variability in commercial core measurements for petrophysical and compositional properties such as porosity, water saturation and mineral concentrations. The deficiencies with the calibration approach as well as the complex rock physics in these reservoirs result in huge uncertainty in well-log-based petrophysical and compositional evaluation of organic-rich source rocks.

New techniques were developed using non-linear inversion methods for joint interpretation of well logs to estimate porosity, TOC (Total Organic Carbon), hydrocarbon saturation, and volumetric concentrations of mineral constituents in the presence of complex mineralogy and thin beds in organic-rich source rocks (Heidari et al., 2012; Heidari et al., 2011). These techniques minimize the calibration effort against core measurements. However, the complex rock physics of organic-rich source rock was missing in many previously introduced well-log interpretation techniques. For instance, assessment of fluid saturations using electrical resistivity logs in conventional reservoirs is traditionally based on resistivity-porosity-saturation models such as Archie's, Dual-Water and Waxman-Smits equations. Conventional resistivity-porosity-saturation models are still commonly used for assessment of fluid saturations using electrical resistivity logs in organic-rich source rocks. All resistivity-porosity-saturation models assume that electrical conductivity in rock fluid systems is only affected by saline water and the presence of clay.

In the case of organic-rich source rocks, however, electrical resistivity of the formation can be affected by conductive mineral such as pyrite and highly mature conductive kerogen in addition to clay minerals and saline water. Therefore, a reliable model for estimating fluid saturations should take into account the effect of all the conductive components in the formation, including kerogen. In highly mature shale-gas reservoirs, the overall electrical resistivity can be 1-2 orders of magnitude less than the measured electrical resistivity in the same formation at relatively lower thermal maturities (Passey et al., 2010). While the organic matter might not be recrystallizing to mineral graphite (which is electrically conductive), there could be intermediary compounds forming. These compounds could have a significant impact on the electrical conductivity in addition to formation water, clay, and pyrite (Passey et al., 2010). The impact of kerogen on electrical resistivity of organic-rich source rocks has not been quantified, yet.

The structural complexity and heterogeneity of kerogen is a hurdle for geochemists aiming to characterize the structural changes in kerogen during thermal maturation. Various analytical methods such as thermal analysis, elemental analysis, degradation methods, fourier transform-infrared spectroscopy (FT-IR), and solid-state nuclear magnetic resonance (NMR) spectroscopy were employed to elucidate some aspects of the structure of kerogen. Among the various methods applied to characterize kerogen, the recently developed advanced solid-state NMR spectroscopy techniques provide much deeper insights into the structures of kerogen (Mao et al., 2010). The increase of aromaticity of kerogen with increasing maturity was well established by numerous NMR

studies (Barwise et al., 1984; Dennis et al., 1982; Miknis et al., 1982, Miknis et al., 1993; Patience et al., 1992; Requejo et al., 1992; Smernik et al., 2006; Solli et al., 1984; Wei et al., 2005; Werner-Zwanziger et al., 2005; Witte et al., 1988). Advanced solid-state NMR studies to characterize the kerogen structure have also provided a correlation between thermal maturity and aromaticity (Mao et al., 2010). The vast delocalization of electrons associated with increasing aromaticity helps in conducting electric current leading to conductive behavior of kerogen. This is also the reason for the electrically conductive nature of graphite that is formed due to recrystallization of carbon in the organic matter. Analytical models (Li et al., 2007) describe the dependence of electrical conductivity of organic semi-conductors on temperature and external electric field. Li et al. (2007) reported electrical resistivity of 1 ohm-m at 170 °F for organic semi-conductors. Electrical conductivity measurements (Rajeshwar et al., 1980) carried out on oil shale samples from the Green River oil shales illustrate the correlation between electrical behavior of organic matter and temperature. Researchers (Meng et al., 2012; Rajeshwar et al., 1980) observed a pronounced effect of thermal maturity of organic matter and temperature on magnitude of measured electrical conductivity of the oil shale samples. The changes in kerogen network and structure, with increasing temperature and maturity, is expected to enhance the electrical conductivity of organic-rich source rock (Meng et al., 2012; Rajeshwar et al., 1980). There is, however, a need for fundamental research to understand the exact mechanism of conduction in such aromatic compounds.

1.2 Statement of the problem

In conventional interpretation techniques, quantitative assessment of hydrocarbon saturations is based on interpreting electrical resistivity logs using conventional resistivity-porosity-saturation models such as Archie's, Dual-Water, and Waxman-Smits equations. However, in organic-rich source rocks, electrical resistivity measurements are affected by presence of highly mature organic matter, pyrite, clays, and complex pore structure in addition to saline connate water.

Characterizing the impact of these factors while interpreting electrical resistivity logs is a major technical challenge. The abundance of highly mature kerogen and conductive minerals such as pyrite in organic-rich source rocks could have a significant impact on electrical resistivity measurements. First, this thesis tries to investigate the possibility of measurable kerogen impact on borehole electrical resistivity measurements.

Another aspect of this thesis focuses on quantifying the impact of various petrophysical and compositional properties of organic-rich source rocks on electrical resistivity and estimates of fluid saturation using pore-scale numerical simulations. This thesis attempts to quantify the effect of volumetric concentration of kerogen, electrical conductivity of kerogen, salt concentration of connate water, kerogen porosity, and spatial connectivity of kerogen-water network on electrical resistivity measurements and estimates of fluid

saturation in organic-rich source rocks. The following section summarizes the goals of the thesis.

1.3 Research objectives

The objectives of this research are as follows:

i. To investigate the reliability of conventional resistivity-porosity-saturation models in assessment of fluid saturations in organic-rich source rocks.

ii. To investigate the possibility of a measurable kerogen impact on electrical resistivity measurements in organic-rich source rocks.

iii. To develop a pore-scale numerical simulation package to model effective electrical resistivity of rock using finite difference methods.

iv. To quantify the impact of various petrophysical, compositional, and electrical properties of organic-rich source rocks on electrical resistivity and estimates of hydrocarbon saturation.

1.4 Outline of the thesis

This thesis consists of five chapters. Following the introductory chapter, Chapter II examines the reliability of conventional resistivity-porosity-saturation models such as Archie's and Dual-Water equations in assessment of fluid saturations in organic-rich source rocks. It provides a conventional workflow to perform joint interpretation of well

logs and core measurements from a well drilled in the Haynesville shale-gas formation. It also investigates the possibility of a measurable impact of volumetric/weight concentration of kerogen on estimation of water saturation from borehole electrical resistivity measurements, based on core measurements and well-log interpretation results.

Chapter III introduces a new petrophysical-compositional-electrical model for organic-rich source rocks. It describes the development of a pore-scale numerical simulator using finite difference methods to solve the steady state Laplace conductivity equation. Chapter IV documents the application of the numerical simulation method to quantify the effect of volumetric concentration of kerogen, electrical conductivity of kerogen, spatial connectivity of kerogen-water network, salt concentration of connate water, and gas-filled kerogen porosity on effective electrical resistivity of pore-scale representations of organic-rich source rocks. It also describes correlations between gas-filled kerogen porosity and effective electrical conductivity of kerogen.

Finally, Chapter V summarizes the contribution of the research stemming from this thesis, draws conclusions based on the results reported, and provides recommendations for future research.

CHAPTER II

RELIABILITY OF CONVENTIONAL RESISTIVITY-POROSITY-SATURATION MODELS

This chapter describes the approach used to perform joint interpretation of well logs from a field example in the Haynesville shale-gas formation. It discusses the workflow used to estimate depth-by-depth petrophysical and compositional properties such as volumetric/weight concentrations of minerals, TOC, porosity, and water saturation. Finally, this chapter examines the reliability of conventional resistivity-porosity-saturation models in providing accurate estimates of fluid saturations in organic-rich source rocks.

2.1 Introduction

The well-log-based assessment of mineralogy, kerogen, porosity, and hydrocarbon saturation in organic-rich source rocks is challenging. It involves many pre-assumptions for physical properties such as density, photoelectric factor, porosity, compressional slowness, and electrical resistivity of pure minerals and fluids in the formation. The workflow presented in this thesis uses core data to decrease non-uniqueness of the results and provides reliable estimates for volumetric/weight concentration of minerals, kerogen, porosity, and water saturation. The accuracy of conventional resistivity-

porosity-saturation models is examined by comparing the fluid saturation estimates against available core measured water saturation.

2.2 An introduction to geology of Haynesville formation

The Haynesville shale in East Texas and Louisiana is one of the most prolific shale-gas plays in the continental United States. Different shale-gas plays exhibit diverse characteristics depending on basin configuration, structural movements, sedimentary input, sea-level fluctuation, and thermal maturity of organic matter. In addition, shale plays within the same basin show similar variations that are significant in terms of thermal maturity of kerogen and need to be considered. As such, the Haynesville shale is characterized by a range in carbonate and silica content, in porosity, in different geochemical characteristics, as well as in different lithofacies types.

The Haynesville mudrocks are classified as mudstones. These fine-grained rocks contain 35% - 57% of clay minerals. The unlaminated siliceous mudstone facies is associated with the highest TOC values, which range between 4% and 8%. The carbonate-rich facies can also have enriched organic matter with TOC weight concentrations of 3% - 5% (Hammes et al., 2009). There is also abundant pyrite throughout in colloidal as well as framboidal forms. Organic matter is predominantly type II/III kerogen, with an average thermal maturity of 1.25% R_o (vitrinite reflectance).

2.3 Method

The input data for the well-log interpretation consisted of wireline logs as well as core measurements. Well logs consisted of gamma ray (GR), neutron porosity, bulk density, array induction resistivity, photoelectric factor (PEF), compressional- and shear-wave velocities, and elemental capture spectroscopy (ECS) logs. The GR log was not used for quantitative evaluation due to significant uncertainties involved with the measurement in organic-rich source rocks caused by the presence and vertical variation of organic matter and matrix impurities. Core measurements in the organic-rich zone consisted of porosity, water saturation, weight concentration of TOC, and x-ray diffraction (XRD) mineralogy data. **Figure 1** shows GR, array induction resistivity, neutron porosity, bulk density, photoelectric factor, and compressional-wave slowness well logs in the selected depth interval in the Haynesville shale-gas formation.

The outcomes of the conventional depth-by depth inversion of well logs include porosity, fluid saturations, volumetric/weight concentration of kerogen, and volumetric/weight concentrations of clay and non-clay minerals. However, due to the complex mineralogy of organic-shale formations, the described inversion was underdetermined, resulting in non-uniqueness of the results.

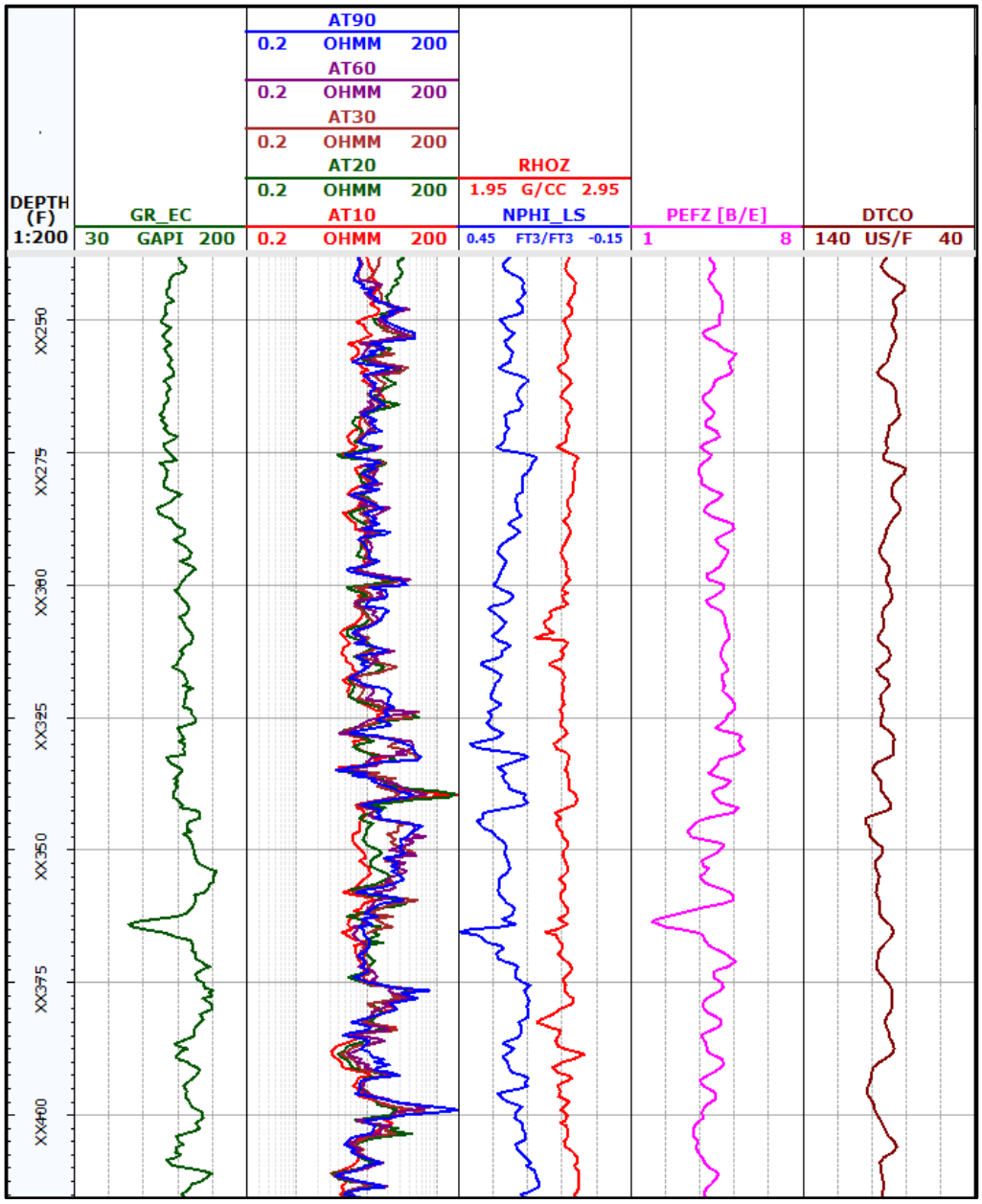

Figure 1: Field Example: Conventional well logs in a well drilled in Haynesville shale-gas formation. Panels from left to right show depth, gamma ray, array induction resistivity, neutron porosity and bulk density, photoelectric factor, and compressional-wave slowness well logs.

To mitigate the non-uniqueness of the results, various techniques were employed based on the workflow introduced by Quirein et al., (2010). The applied techniques included (a) decreasing the number of unknown mineral components in the assumed petrophysical/compositional rock model, (b) applying constraints based on correlations between volumetric concentrations of minerals, and (c) using a pre-calculated depth-by-depth volumetric concentration of kerogen as an input curve to constrain the joint inversion.

2.3.1 Define petrophysical and compositional model

The number of unknown mineral components in the assumed petrophysical/compositional model was originally determined using core XRD bulk mineralogy data. Next, minerals with less than 2.5% volumetric concentration were eliminated from the initial petrophysical model. Finally, minerals with similar physical properties such as illite-mica and mixed layer clay were lumped together. The assumed components in the final petrophysical/compositional model included:

(a) Non-clay minerals comprising of quartz, plagioclase, calcite, dolomite, and pyrite,

(b) Illite as the only clay mineral,

(c) Kerogen, and

(d) Fluids including gas and saline water.

Figure 2 shows the final petrophysical/compositional model assumed for well-log interpretation.

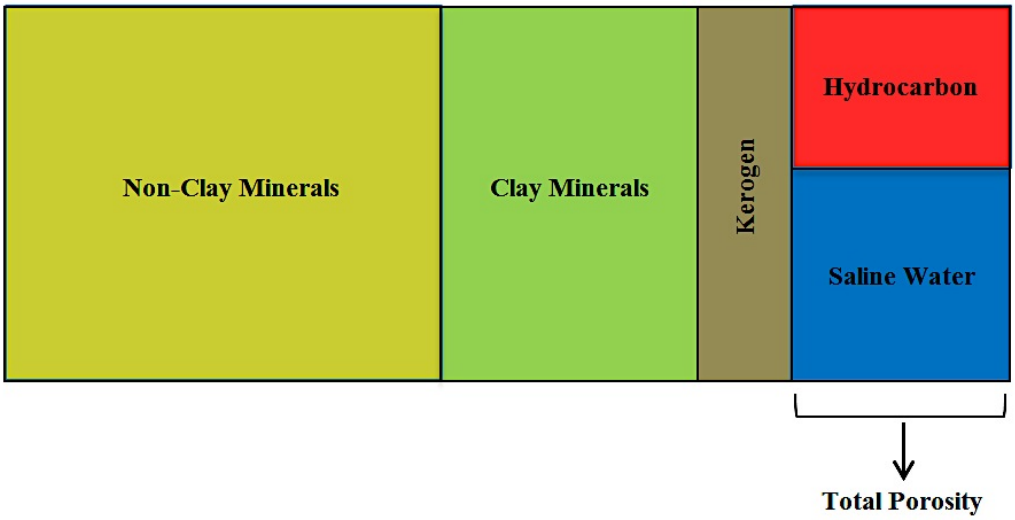

Figure 2: Assumed petrophysical/compositional rock model for organic-rich source rocks used for well-log interpretation.

2.3.2 Establishing constraints between volumetric concentrations of minerals

Analysis of the core XRD data revealed a linear correlation between volumetric concentrations of plagioclase and quartz (**Figure 3**). The linear correlation between volumetric concentrations of plagioclase and quartz was given by

$$C_{Plagioclase} = 0.133 C_{Quartz} + 1.824 \ , \qquad (1)$$

where $C_{Plagioclase}$ is the volumetric concentration of plagioclase and C_{Quartz} is the volumetric concentration of quartz. This linear correlation was used as an equality constraint in the inversion of well logs.

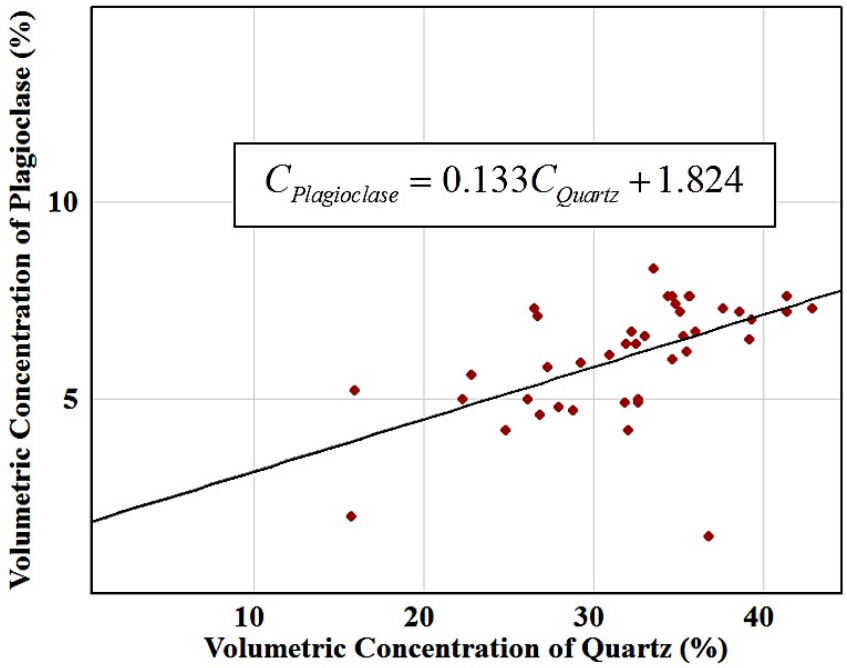

Figure 3: Correlation between volumetric concentration of plagioclase and quartz obtained from core measurements.

2.3.3 Assessment of volumetric concentration of kerogen

A depth-by-depth volumetric concentration of kerogen, separately calculated using ΔlogR method (Passey et al., 1990), was used as an input curve to constrain the joint inversion of well logs. First, the density of organic matter was estimated using a simple

crossplot of the inverse core grain density and the TOC weight concentration from core data. The correlation between the grain density and the weight concentration of TOC was given by

$$1/\rho_{grain} = 0.0048TOC + 0.35 \ , \tag{2}$$

where ρ_{grain} is the core grain density and TOC is the weight concentration of TOC from core data. From this correlation, a value of 1.2 g/cc was obtained for density of organic matter, which was used in the model parameters for the joint inversion of input well logs. **Figure 4** shows the correlation between inverse core-measured grain density and TOC weight concentration obtained from core data.

Next, depth-by-depth weight concentration of TOC was estimated using the ΔlogR technique developed by Passey (1990). This method uses array induction deep resistivity well logs and acoustic compressional-wave slowness well logs to estimate weight concentration of TOC. The resistivity and compressional-wave slowness well logs were overlain and baselined in a "non-source" rock closest to the zone of interest. With the baseline established, organic-rich intervals were recognized based on the separation between the two logs. The separation between the deep resistivity and compressional-wave slowness well logs was measured and a depth-by-depth ΔlogR curve was generated.

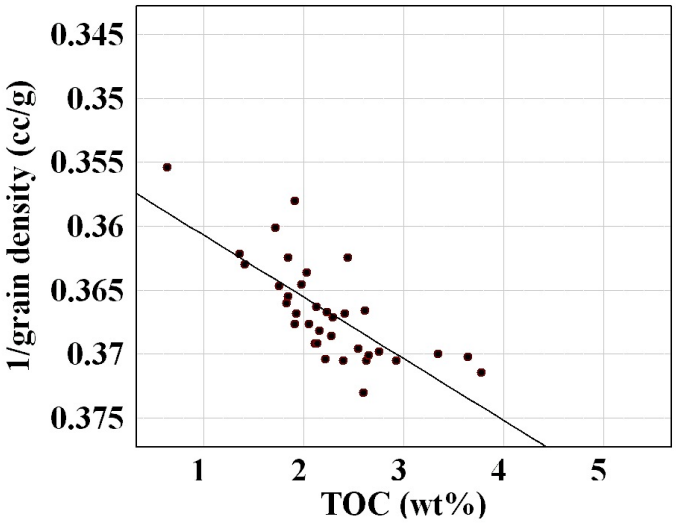

Figure 4: Correlation between weight concentration of TOC from core and inverse of core grain density.

ΔlogR was calculated via (Passey et al., 1990)

$$\Delta \log R = \log(R/R_{baseline}) + 0.02(\Delta t - \Delta t_{baseline}) \ , \tag{3}$$

where R is the resistivity measurement in ohm-m, Δt is the measured compressional-wave slowness in μsec/ft, $R_{baseline}$ is the resistivity value corresponding to the $\Delta t_{baseline}$ value when the well logs are baselined in the non-source rock zone.

The ΔlogR separation is linearly related to TOC and is a function of thermal maturity of the organic matter. The empirical equation used to calculate TOC from ΔlogR was given by (Passey et al., 1990)

$$W_{TOC} = (\Delta \log R) \times 10^{(2.297 - 0.1688\,LOM)}\ , \tag{4}$$

where W_{TOC} is the weight concentration of total organic carbon content and LOM is the level of maturity. **Figure 5** shows the resistivity, compressional-wave slowness, and depth-by-depth estimates of TOC weight concentration.

Next, an empirical correlation was obtained from regression of core weight concentration of TOC and core volumetric concentration of kerogen given by

$$C_k = 2.234 W_{TOC} + 0.089\ , \tag{5}$$

where C_k is the volumetric concentration of kerogen and W_{TOC} is the weight concentration of TOC.

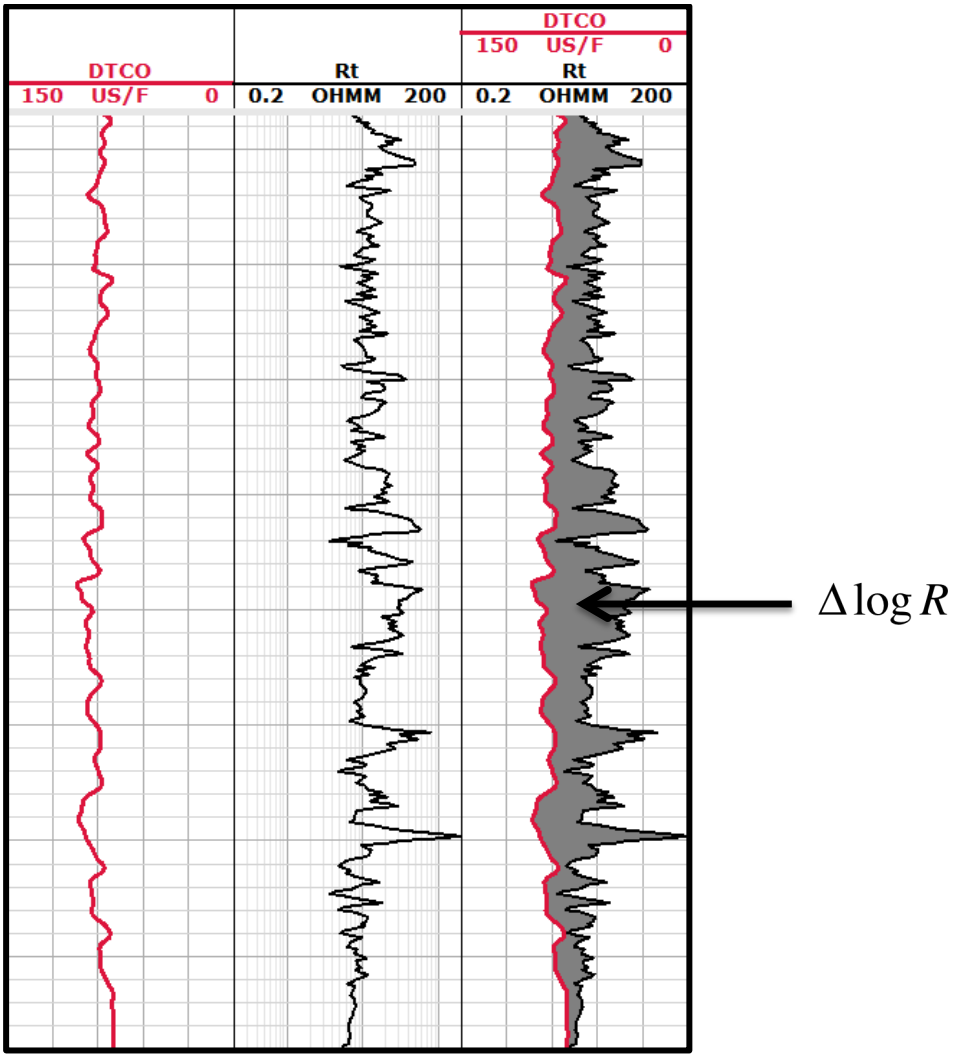

Figure 5: Overview of the ΔlogR method. Panels from left to right show compressional-wave slowness, array induction deep resistivity, and the separation between the two after defining the baseline.

Finally, a depth-by-depth volumetric concentration of kerogen was estimated from the weight concentration of TOC calculated using the ΔlogR method. **Figure 6** shows the crossplot of weight concentration of TOC versus volumetric concentration of kerogen obtained from core data. The estimated volumetric concentration of kerogen was used as a constraint in the joint inversion of well logs.

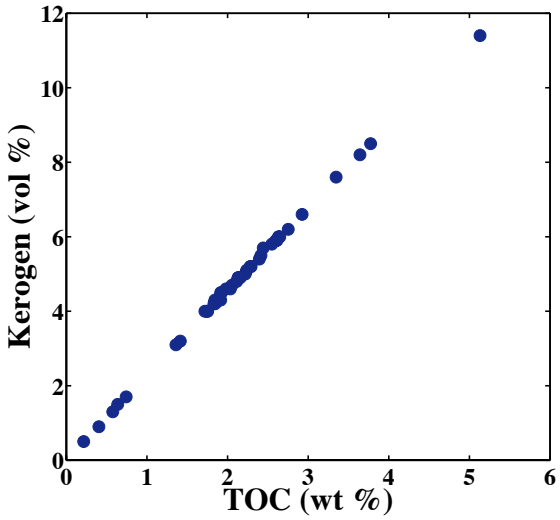

Figure 6: Crossplot of volumetric concentration of kerogen and weight concentration of TOC from core measurements.

2.4 Joint interpretation of well logs

The application of constraints, in addition to the optimized mineral model, reduced the non-uniqueness of the results in joint inversion of well logs. This resulted in an even-

determined inversion. Commercial software was used to perform joint inversion of well logs to assess the depth-by-depth petrophysical and compositional properties of the formation. Input well logs to the inversion included array induction resistivity, bulk density, neutron porosity, photoelectric factor, compressional-wave slowness, and ECS logs. The outputs included volumetric concentrations of minerals, porosity, and water saturation. Dual Water model, a conventional resistivity-porosity-saturation model, was used as part of the joint interpretation of well logs to estimate fluid saturations. The inversion parameters were calibrated based on comparison of well-log interpretation results against available core measurements. The Archie's parameters in Dual-water model were estimated by calibration against core porosity and water saturation in depth intervals with minimal TOC.

Well-log interpretation results showed good agreement with core data for porosity and volumetric/weight concentrations of minerals (**Figure 7**). However, significant relative errors of 20% - 40% in estimates of water saturation (compared to water saturation obtained from core measurements) were observed in zones with high volumetric concentration of kerogen (**Figure 8**). These results suggested a significant impact of highly mature kerogen on estimates of fluid saturations using conventional resistivity-porosity-saturation models. In addition to high volumetric concentration of mature kerogen in these zones, the presence of pyrite associated with kerogen could also be responsible for the error in estimates of water saturation.

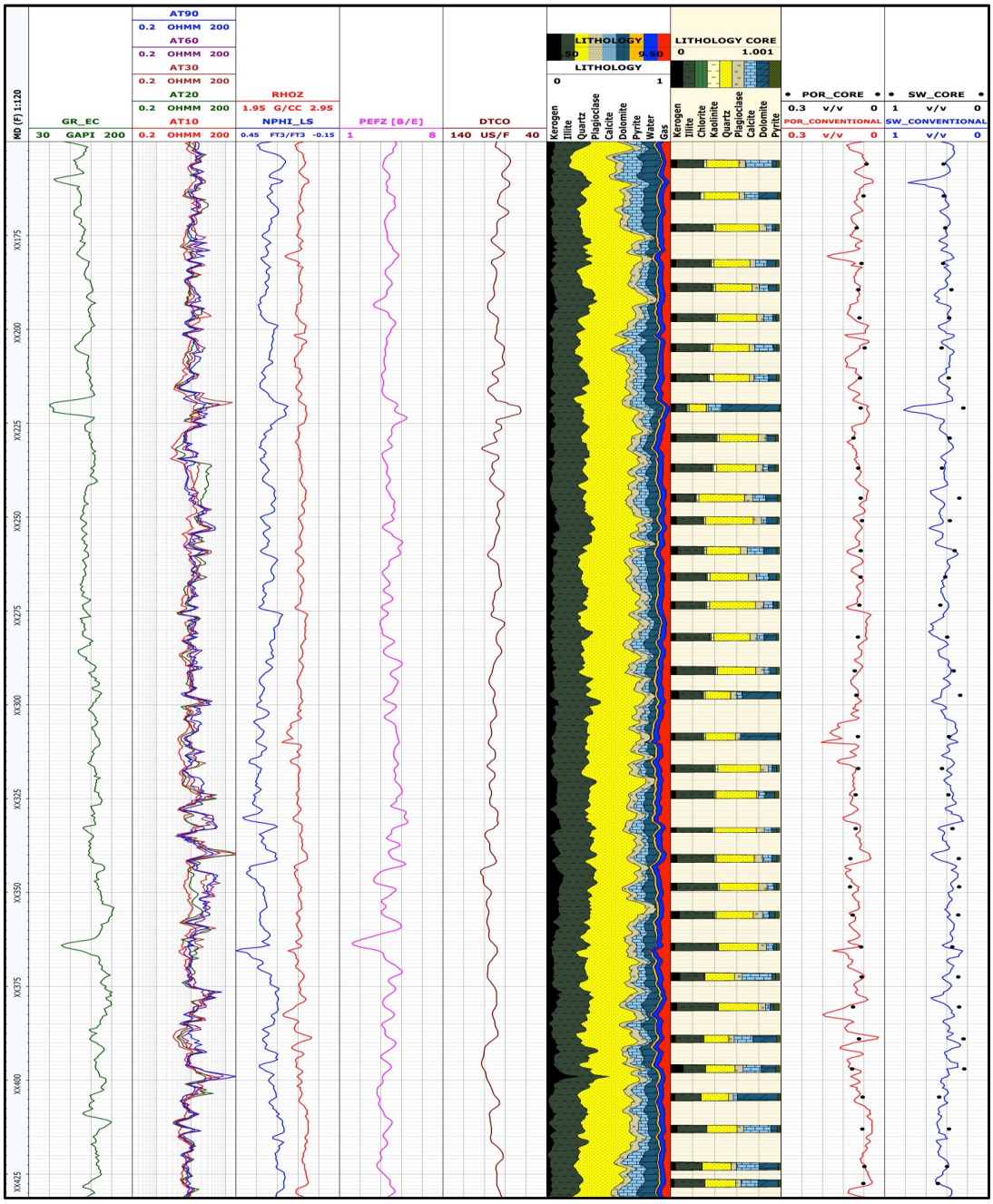

Figure 7: Field Example: Comparison of the results obtained from well-log interpretation against core measurements for total porosity (ninth left-hand panel), total water saturation (tenth left-hand panel), volumetric concentrations of mineral constituents (seventh left-hand panel), and volumetric concentration of minerals obtained from core measurements (eighth left-hand panel). Panels from left to right show depth, gamma ray, array induction resistivity, neutron porosity and density, PEF, and compressional-wave slowness logs.

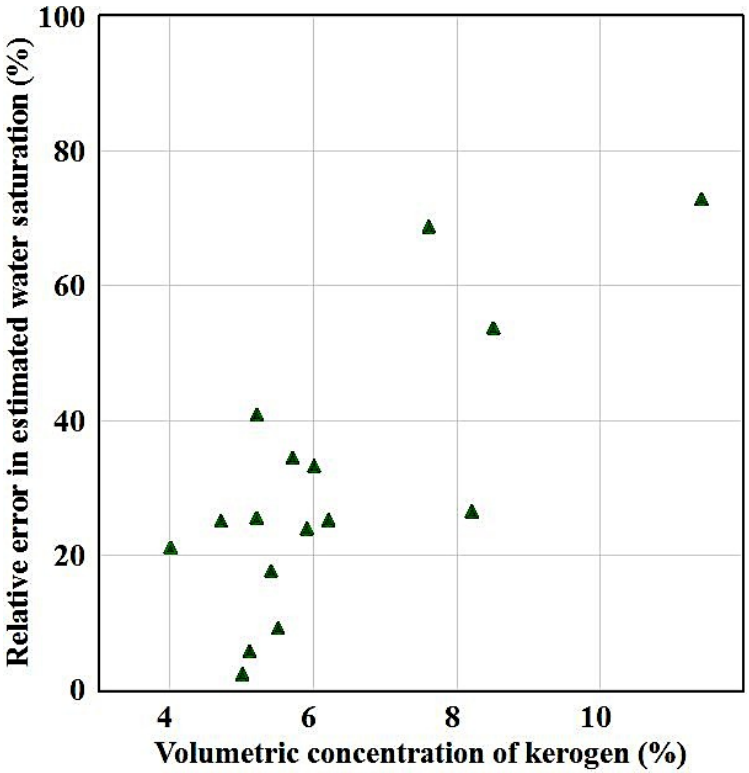

Figure 8: Crossplot of relative error in estimates of water saturation and volumetric concentration of kerogen.

CHAPTER III

METHOD

This chapter presents a pore-scale numerical simulation approach for assessment of effective electrical resistivity of rock-fluid media. In this approach, a digital porous medium was created based on SEM (scanning electron microscopy) images of rock in organic-rich source rock formations. Then, a numerical simulator was developed for assessment of electric field, electric currents, and effective electrical resistivity in 2D (two-dimensional) and 3D (three-dimensional) pore-scale images. This chapter discusses the numerical simulation method developed to solve the Laplace conductivity equation based on a finite difference approach. It also presents the petrophysical and electrical rock model used for pore-scale numerical simulations in organic-rich source rocks.

The first section in this chapter provides the theoretical basis behind simulation of electrical conduction phenomena at the pore-scale level in porous media. Section 3.2 describes the modeling process and the development of the finite difference based numerical simulator. Section 3.3 discusses the methodology used to develop 2D and 3D synthetic images of organic-rich source rocks. It develops a petrophysical/compositional rock model assumed for pore-scale numerical simulations based on petrophysical, compositional, and electrical properties of rock constituents.

3.1 Introduction

For a steady state conductivity problem, where the currents are steady in time, the charge conservation equation is given by

$$\nabla \cdot \vec{J} = 0 \ , \tag{6}$$

where $\nabla \cdot$ is the divergence operator and $\vec{j}$ is the electric displacement field. The constitutive equation is given by

$$\vec{J} = \sigma \vec{E} \ , \tag{7}$$

where σ is the electrical conductivity of the medium and $\vec{E}$ is the electric field. The electric field can be expressed in terms of the scalar electric potential via

$$\vec{E} = -\nabla V \ , \tag{8}$$

where V is the electric field potential. **Equations 7** and **8** can be substituted in **Equation 6** to give

$$-\nabla \cdot (\sigma \nabla V) = 0 \, . \tag{9}$$

Equation 9 is known as the differential form of the Laplace steady state conductivity equation. This second order Partial Differential Equation (PDE) can be discretized into a set of linear, simultaneous equations. The following section describes the finite difference discretization of the Laplace conductivity equation.

3.2 Finite difference method

Finite difference methods have dominated computational science since its inception and are still utilized for a wide array of computational engineering and science problems. Briefly, the method can be characterized as follows:

(i) It utilizes uniformly spaced grids.

(ii) Derivatives at each node are numerically approximated using a finite difference stencil.

(iii) A system of equations is obtained by evaluating the previous step for each node.

(iv) The system of equations is solved for the electric field potential, which is the dependent variable.

The Laplace equation in cartesian coordinates can be expressed as

$$-\left(\frac{\partial(\sigma\nabla V)_x}{\partial x}+\frac{\partial(\sigma\nabla V)_y}{\partial y}+\frac{\partial(\sigma\nabla V)_z}{\partial z}\right)=0 \quad . \tag{10}$$

Equation 10 was discretized using Taylor series. Given a function *f(x)*, the second order, central difference approximation of the second derivative, *f"(x)* can be expressed as

$$\frac{d^2 f}{dx^2} = \frac{f(x-\Delta x) - 2f(x) + f(x+\Delta x)}{\Delta x^2} + O(\Delta x^2) \ , \tag{11}$$

where Δx represents the increment in x and $O(\Delta x^2)$ is the error of approximation.

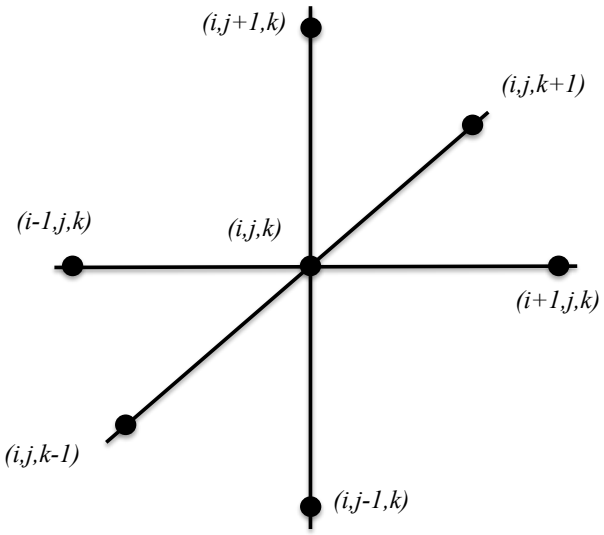

Figure 9: Seven-point finite difference stencil used for discretization of the Laplace conductivity equation in a 3D domain.

The finite difference approximation of the second order Laplace's equation on a cartesian grid was derived using a seven-point finite difference 3D stencil as shown in **Figure 9**.

Next, the differential form was discretized expanding each term via

$$\frac{\partial(\sigma\nabla V)_x}{\partial x} = \frac{(\sigma_{i+1,j,k}+\sigma_{i,j,k})(V_{i+1,j,k}-V_{i,j,k})-(\sigma_{i,j,k}+\sigma_{i-1,j,k})(V_{i,j,k}-V_{i-1,j,k})}{2\Delta x^2}\ , \qquad (11)$$

$$\frac{\partial(\sigma\nabla V)_y}{\partial y} = \frac{(\sigma_{i,j+1,k}+\sigma_{i,j,k})(V_{i,j+1,k}-V_{i,j,k})-(\sigma_{i,j,k}+\sigma_{i,j-1,k})(V_{i,j,k}-V_{i,j-1,k})}{2\Delta y^2}\ , \qquad (12)$$

and

$$\frac{\partial(\sigma\nabla V)_z}{\partial z} = \frac{(\sigma_{i,j,k+1}+\sigma_{i,j,k})(V_{i,j,k+1}-V_{i,j,k})-(\sigma_{i,j,k}+\sigma_{i,j,k-1})(V_{i,j,k}-V_{i,j,k-1})}{2\Delta z^2}\ , \qquad (13)$$

where $\sigma_{i,j,k}$ is the local conductivity at location *(i,j,k)*, $V_{i,j,k}$ is the electric potential at location *(i,j,k)*, and Δx, Δy, and Δz represent the increments in x, y, and z directions, respectively. Next, the PDE in **Equation 11** was expressed as a set of linear, simultaneous equations given by

$$\left(\frac{(\sigma_{i-1,j,k}+2\sigma_{i,j,k}+\sigma_{i+1,j,k})}{2\Delta x^2}+\frac{(\sigma_{i,j-1,k}+2\sigma_{i,j,k}+\sigma_{i,j+1,k})}{2\Delta y^2}+\frac{(\sigma_{i,j,k-1}+2\sigma_{i,j,k}+\sigma_{i,j,k+1})}{2\Delta z^2}\right)V_{i,j,k} -$$
$$\frac{(\sigma_{i-1,j,k}+\sigma_{i,j,k})V_{i-1,j,k}+(\sigma_{i,j,k}+\sigma_{i+1,j,k})V_{i+1,j,k}}{2\Delta x^2} -$$
$$\frac{(\sigma_{i,j-1,k}+\sigma_{i,j,k})V_{i,j-1,k}+(\sigma_{i,j,k}+\sigma_{i,j+1,k})V_{i,j+1,k}}{2\Delta y^2} -$$
$$\frac{(\sigma_{i,j,k-1}+\sigma_{i,j,k})V_{i,j,k-1}+(\sigma_{i,j,k}+\sigma_{i,j,k+1})V_{i,j,k+1}}{2\Delta z^2}=0. \qquad (14)$$

The electric field potential at each node point was obtained as a solution to the linear system of equations in **Equation 15** expressed as

$$KV = B\,, \tag{15}$$

where K is the stiffness matrix representing the matrix comprised of the coefficients to the electric potential terms, B represents the matrix comprised of elements derived from the boundary conditions imposed on the problem, and V is the matrix comprised of the electric potentials at each node. The solution to **Equation 16** was derived by solving for spatial distribution of electric field potential using either direct or iterative methods.

3.2.1 Boundary conditions

Solution to **Equation 16** requires the specification of certain conditions that the electric field potential must satisfy at the boundary of the 3D domain. A preset electric potential was applied on two opposite boundaries and imposed Dirichlet boundary conditions. Furthermore, no electric current flow was assumed across the other boundaries and Neumann boundary conditions were imposed at these boundaries. While the Dirichlet boundary conditions were incorporated in the matrix B, imposing Neumann boundary conditions was challenging.

Figure 10 shows the mesh generated over a slice of the 3D domain. The total number of nodes in x, y, and z directions are m, n, and p respectively. For the Dirichlet nodes (shown in green), the electric potential at nodes on the left boundary was given by

$$V_{i,1,k} = V_{left} \ , \tag{16}$$

where $V_{i,1,k}$ is the electric potential on the nodes at j = 1 and V_{left} is the preset constant electric potential on the left boundary.

Similarly, electric potential at nodes on the right boundary was given by

$$V_{i,n,k} = V_{right} \ , \tag{17}$$

where $V_{i,n,k}$ is the electric potential on the nodes at j = n and V_{right} is the preset constant electric potential on the right boundary. Therefore, the assumed potential difference between the right and left boundaries was calculated via

$$\Delta V = V_{left} - V_{right} \ . \tag{18}$$

For the Neumann nodes (red nodes in **Figure 10**), the derivative of electric potential in the direction normal to the boundary is zero, expressed via

$$\left(\frac{\partial V_{i,j,k}}{\partial y}\hat{j}\right)_{i=1} \bullet (-\hat{j}) = 0 \ , \tag{19}$$

and

$$\left(\frac{\partial V_{i,j,k}}{\partial y}\hat{j}\right)_{i=m} \bullet \hat{j} = 0 \ . \tag{20}$$

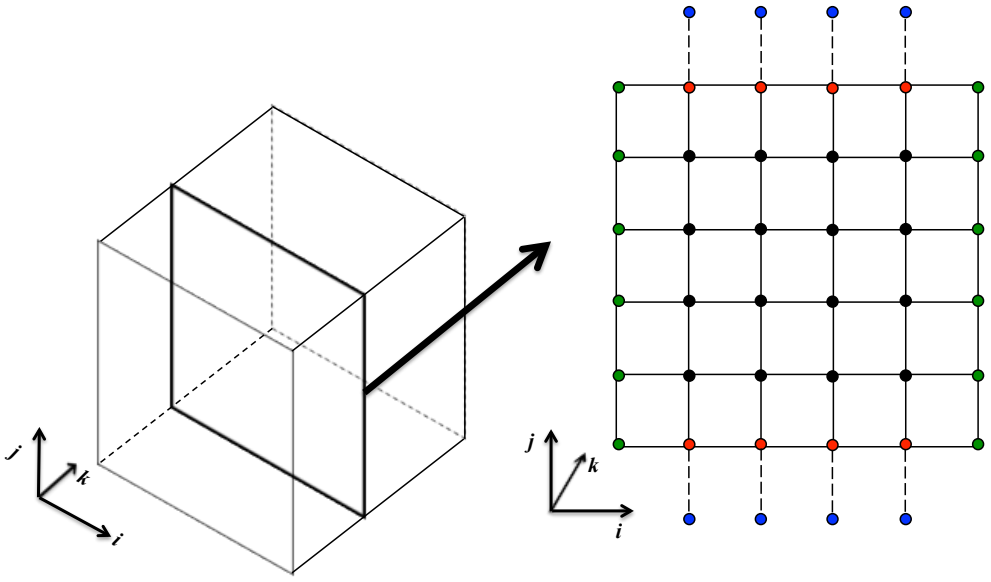

(a) (b)

Figure 10: (a) Sample 3D domain and (b) grid generated over a 2D section. Circles in green, red, and blue represent Dirichlet nodes, Neumann nodes, and ghost nodes, respectively.

The nodes on i = 1 and i = m are, however, boundary nodes and electric potentials $V_{i-1,j,k}$ and $V_{i+1,j,k}$, for central difference discretization of **Equations 20** and **21** are not present in the domain. To enforce the Neumann boundary condition, the concept of ghost nodes

was used. Ghost nodes (blue nodes in **Figure 10**) were imagined outside the domain and the central difference approximation at $i = 1$, $i = m$, $k = 1$, and $k = p$ was evaluated to impose the boundary condition.

3.2.2 Node-numbering

First, the linear system of equations given by **Equation 15** was derived for internal nodes and the nodes under Dirichlet and Neumann boundary conditions. Next, a node-numbering scheme was developed to assemble the stiffness matrix, K, and matrix B. **Figure 11** shows an example of the node-numbering scheme in a 6x6x6 3D domain. It illustrates the node-numbers over two subsequent 2D faces of the 3D domain.

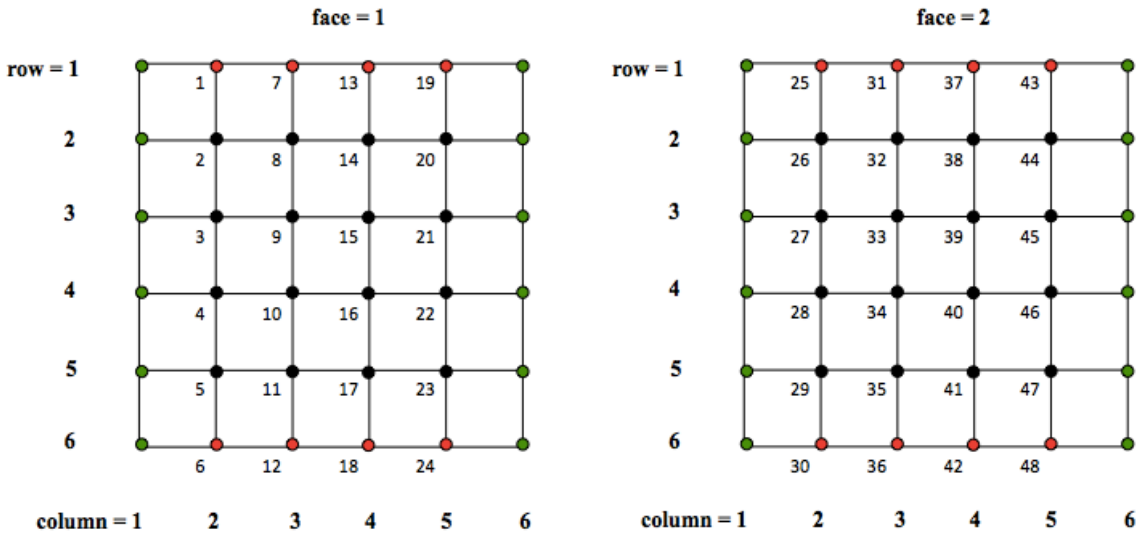

Figure 11: Mesh generated over two subsequent 2D faces of the 6x6x6 3D domain. The nodes are referenced in a row, column, and face format. Circles in green and red represent Dirichlet nodes and Neumann nodes, respectively.

The stiffness matrix, *K*, was assembled using the coefficients of the electric potential terms in **Equation 15**. For instance, consider the 3D finite difference stencil around a node given by *(row,column,face)* as shown in **Figure 12**. The stiffness matrix was then populated with the coefficients for each grid point placed at the appropriate position based on the node-numbering scheme illustrated in **Figure 11**.

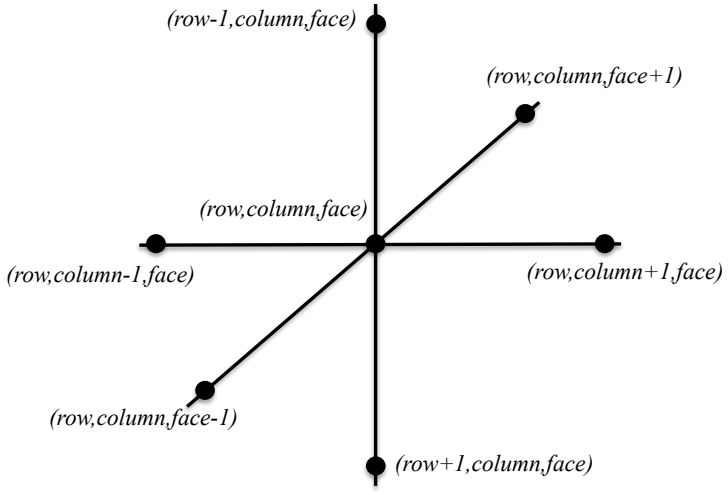

Figure 12: Seven-point finite difference stencil in 3D for a node referenced in row, column, and face matrix notation.

3.2.3 Summary

The stiffness matrix in this problem was a sparse matrix, leading to an ill-conditioned inverse problem. Iterative method was used to optimize computational time and solve the system of simultaneous equations for the electric field potential at each grid point.

For numerical simulations in the 3D pore-scale images, the quasi-minimal residual method (QMR) was used to solve for the electric potential, iteratively.

The 3D numerical simulator was developed to model steady state electrical flow through the porous medium. The cell-centered finite difference code was developed in MATLAB®. The input to the simulator includes (a) digitized pore-scale image of rock-fluid system, (b) electrical resistivity of each matrix/fluid component, and (c) assumed potential difference between two opposite boundaries of the image. The simulator solves for the spatial distribution of electric field potential with a preset potential difference at two opposite boundaries of the porous medium. The other boundaries were assumed to be no-flow boundaries. Next, the spatial distribution of electrical current was computed through the porous medium and effective electrical resistivity of the 3D domain was then derived using Ohm's law. To optimize the number of grids and consequently CPU (Central Processing Unit) time, grid size was progressively decreased until a variation of less than 0.25% in the estimated electrical resistivity was achieved. However, the grid size can be variable in different cases with different spatial distribution of fluids, grains, and kerogen. The following section describes the assumed petrophysical/compositional rock model and segmentation method used to build synthetic images of organic-rich source rock.

3.3 The assumed petrophysical/compositional rock model

The inputs for the numerical simulations were synthetic digital representations of organic-rich source rock. Synthetic images of the rock-fluid system were developed based on SEM images of organic-rich source rock in order to capture the spatial distribution of organic matter and porosity of the rock. For instance, rock images in the Haynesville shale-gas formation were used to model dispersed spatial distribution of kerogen, and rock images in the Woodford shale-gas formation were used to represent layered spatial distribution of kerogen. The 2D digital images were segmented to define matrix/fluid constituents including non-conductive matrix, kerogen, brine, and hydrocarbon. Furthermore, 3D synthetic images of organic-rich source rocks were developed using random walk and random distribution algorithms to spatially distribute kerogen and pore space. 3D images can also be developed using 3D FIB-SEM (Focused Ion Beam-Scanning Electron Microscopy) images, if available. **Figure 13** describes the assumed petrophysical rock model used to segment the digital images. This assumed petrophysical/compositional model includes non-conductive matrix, conductive minerals such as pyrite, kerogen, gas within kerogen, and saline water.

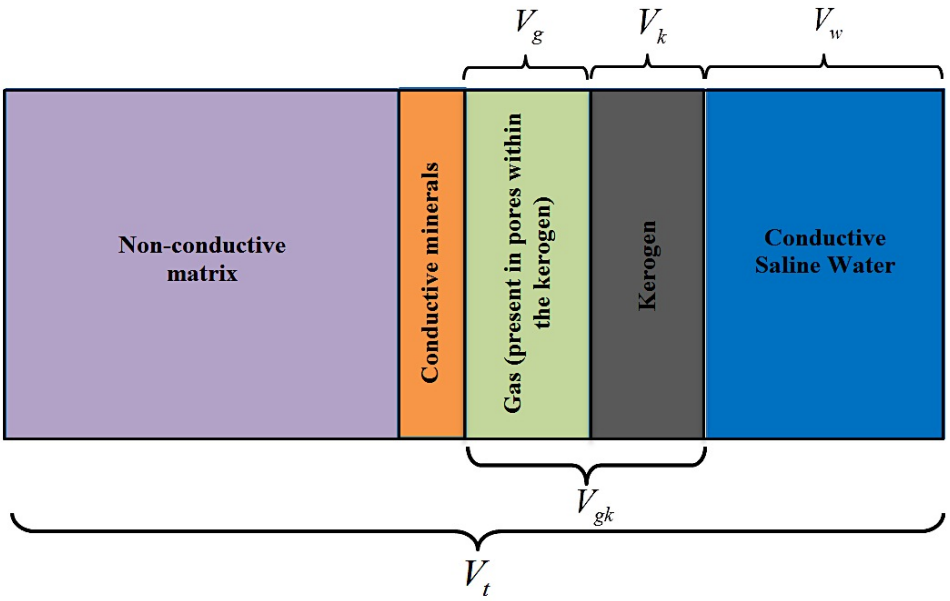

Figure 13: Assumed petrophysical/compositional rock model designed based on electrical properties of rock and fluid constituents adopted for pore-scale numerical simulations.

In the assumed petrophysical/compositional rock model, the water and gas saturations is given by

$$S_w = \frac{V_w}{V_w + V_g} \tag{22}$$

and

$$S_g = \frac{V_g}{V_w + V_g} \ , \tag{23}$$

respectively, where V_w is the volume of water, V_g is the volume of gas within kerogen, S_w is the water saturation, and S_g is the gas saturation.

The volumetric concentration of kerogen, C_k, is given by

$$C_k = \frac{V_k}{V_t} \ , \tag{24}$$

where V_k is the volume of kerogen and V_t is the total rock volume. The kerogen porosity, ϕ_k, is expressed as

$$\phi_k = \frac{V_g}{V_{gk}} \ , \tag{25}$$

where V_{gk} represents the net volume of gas-bearing kerogen and is given by

$$V_{gk} = V_g + V_k \ . \tag{26}$$

The total porosity of the rock-fluid system, ϕ_t, is defined as

$$\phi_t = \frac{V_g + V_w}{V_t} \ . \tag{27}$$

CHAPTER IV

PORE-SCALE NUMERICAL SIMULATIONS OF ELECTRICAL RESISTIVITY IN ORGANIC-RICH SOURCE ROCKS

This chapter documents the application of the numerical simulation method described in Chapter III in four synthetic cases. Pore-scale numerical simulations were used to quantify the impact of volumetric/weight concentration of kerogen, kerogen electrical conductivity, kerogen porosity, and spatial connectivity of kerogen-water network on effective electrical resistivity of organic-rich source rocks. Finally, the chapter presents the possible improvement in estimates of fluid saturations using resistivity-porosity-saturation models by taking into account the effect of kerogen on electrical resistivity measurements. The first synthetic case presents a sensitivity analysis to quantify the effect of electrical conductivity, spatial distribution, and volumetric concentration of kerogen on electrical resistivity in 2D images of organic-rich source rock. The second synthetic case is used to investigate the impact of spatial connectivity of kerogen-water network on electrical resistivity in 3D images of organic-rich source rock. The third synthetic case quantifies the correlation between gas-filled kerogen porosity and electrical conductivity of kerogen. Finally, the fourth synthetic case shows the improvement in estimates of fluid saturations in organic-rich source rocks by taking into account the effect of conductive gas-saturated kerogen.

4.1 Synthetic Case No. 1: Effect of kerogen conductivity and volumetric concentration of kerogen on electrical resistivity of organic-rich source rocks

In this synthetic case, 2D images of rock-fluid systems were developed based on field examples in the Haynesville and Woodford shale-gas formations. SEM images from the Haynesville and Woodford shale-gas formations were segmented to develop dispersed and layered spatial distributions of kerogen, respectively (**Figure 14)**. The segmented images consisted of non-conductive grains, conductive brine, and kerogen. **Table 1** lists the assumed total porosity, water saturation, and electrical resistivity for different components in the petrophysical/compositional rock model.

The matrix pore space was saturated with saline water and kerogen porosity was assumed to be zero. The electrical resistivity of kerogen was varied over a wider range from 10^7 ohm-m to 1 ohm-m (non-conductive to highly conductive) to quantify the influence of kerogen conductivity on effective electrical resistivity of the rock-fluid system.

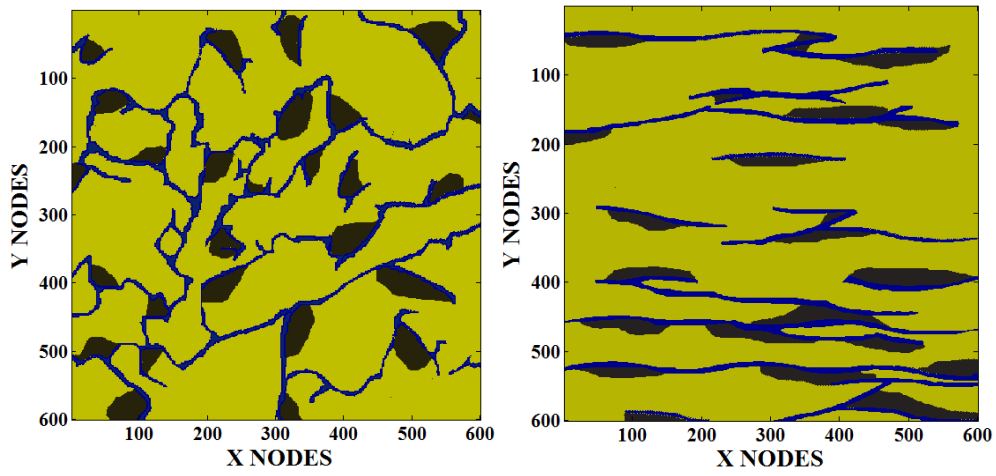

(a) (b)

Figure 14: Synthetic Case No. 1: Two-dimensional pore-scale images of (a) dispersed and (b) layered spatial distributions of kerogen. Yellow, blue, and black areas represent grains, water, and kerogen, respectively.

Table 1: Synthetic Case No. 1: Summary of the petrophysical, electrical, and modeling parameters.

Variable	**Value**	**Units**
Grid size	41.7	nm
Domain size	25 x 25	μm
Total porosity	10	%
Water saturation	100	%
Formation temperature	175	°F
Resistivity of grains	10^7	ohm-m
Resistivity of connate water at 175 °F	0.05	ohm-m
Resistivity of kerogen at 175 °F	1 - 10^7	ohm-m

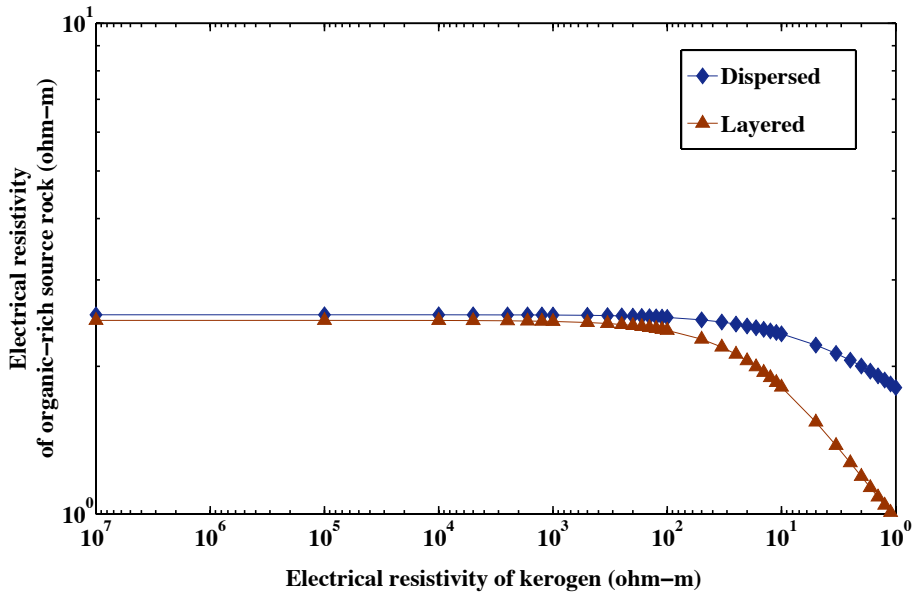

Figure 15: Synthetic Case No. 1: Comparison of the impact of kerogen conductivity on electrical resistivity of organic-rich source rocks. Blue and red lines show estimated effective rock electrical resistivity in the synthetic cases with dispersed and layered kerogen distributions, respectively.

Figure 15 shows the sensitivity of effective electrical resistivity of the rock-fluid system to electrical conductivity of kerogen for both dispersed and layered spatial distributions of kerogen. Results suggest that for kerogen electrical resistivity greater than 100 ohm-m, the electrical resistivity of rock remains unaffected by the presence of kerogen. Furthermore, there is a sharper decrease in electrical resistivity of rock in the case with layered distribution of kerogen compared to the case with dispersed distribution of kerogen. The sharper decrease in the case of layered kerogen distribution is due to the greater kerogen network connectivity.

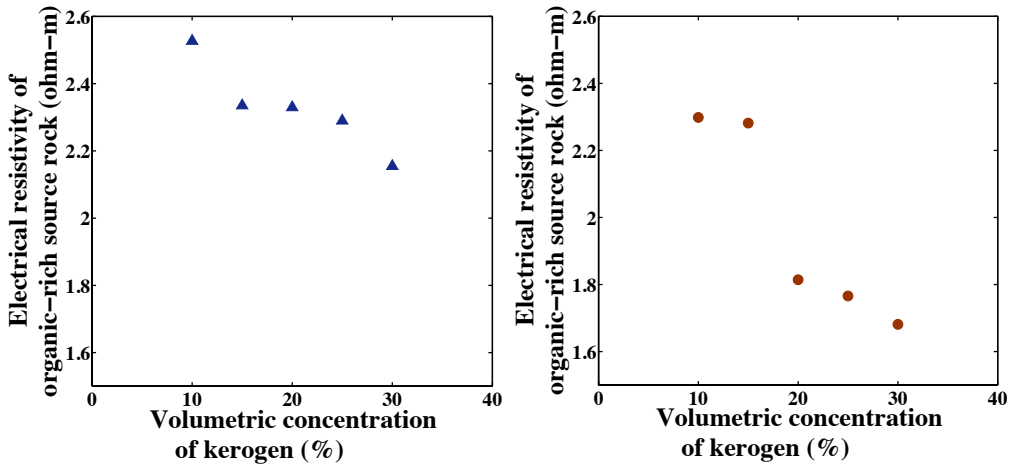

(a) (b)

Figure 16: Synthetic case I: Sensitivity analysis on the impact of volumetric concentration of kerogen on effective rock electrical resistivity of organic-rich source rock in (a) dispersed and (b) layered spatial distribution of kerogen.

Next, a sensitivity analysis was performed to quantify the effect of volumetric concentration of kerogen on electrical resistivity of the rock-fluid system. The volumetric concentration of kerogen was varied from 10% to 30%. **Figure 16** shows the sensitivity analysis of electrical resistivity to volumetric concentration of kerogen for dispersed and layered cases, respectively. The matrix porosity was assumed to be 10% and was fully saturated with saline water. In both cases electrical resistivity of rock-fluid system decreased with increase in volumetric concentration of kerogen. A significant drop in estimated electrical resistivity was observed at 15% and 20% volumetric concentration of kerogen in the dispersed and layered cases, respectively. The more

significant decrease in electrical resistivity in the case of layered kerogen is due to the increase in connectivity of kerogen network.

In the next synthetic case, numerical simulations were performed to quantify the impact of spatial distribution and connectivity of kerogen-water network in 3D images of organic-rich source rocks.

4.2 Synthetic Case No. 2: Impact of kerogen spatial distribution and connectivity of kerogen-water network on electrical resistivity of organic-rich source rocks

In addition to volumetric concentration and conductivity of kerogen, the connectivity of kerogen and water phase can have a significant impact on electrical resistivity measurements. Synthetic Case No. 2 examines the impact of kerogen and water phase connectivity on electrical resistivity of organic-rich source rocks.

First, a sensitivity analysis was run to investigate the effect of kerogen conductivity on electrical resistivity of 3D image of organic-rich source rock, where kerogen network is connected. A synthetic 3D pore-scale image of the rock-fluid system was developed with 20% volumetric concentration of kerogen and 5% matrix porosity fully saturated with saline water (**Figure 17**).

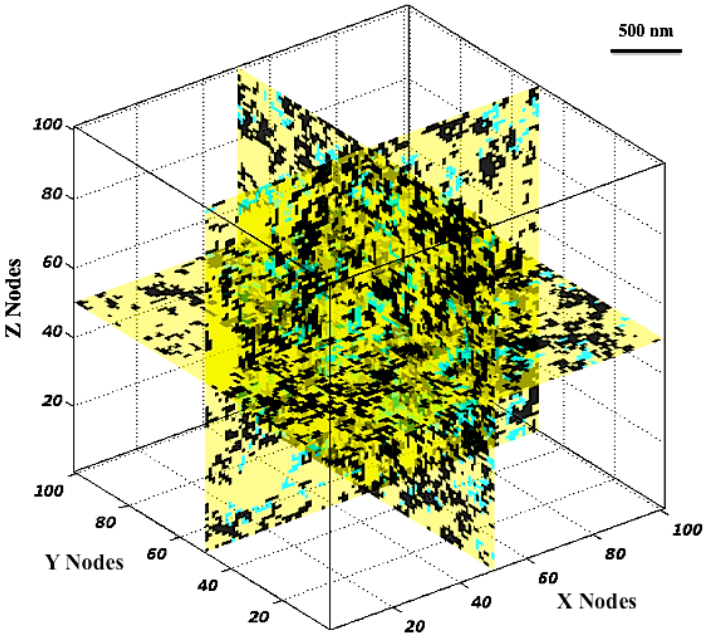

Figure 17: Synthetic Case No. 2: Three-dimensional pore-scale image of organic-rich source rock. Yellow, blue, and black areas represent grains, water, and kerogen, respectively.

Table 2 lists the petrophysical, compositional, and electrical parameters assumed in the numerical simulations. The electrical resistivity of kerogen was progressively decreased from 10^7 ohm-m to 1 ohm-m to examine the effect on effective electrical resistivity of synthetic 3D pore-scale image of organic-rich source rock. **Figure 18** shows the results of the sensitivity analysis. With the increase in connectivity of kerogen network in the synthetic 3D image, there was an increased sensitivity of electrical resistivity of the rock to kerogen conductivity, compared to Synthetic Case No. 1. The impact of kerogen on electrical resistivity of organic-rich source rock was observed at 1000 ohm-m electrical

resistivity of kerogen in Synthetic Case No. 2 compared to 100 ohm-m in Synthetic Case No. 1.

Table 2: Synthetic case II: Summary of the assumed petrophysical, electrical, and modeling parameters.

Variable	**Value**	**Units**
Grid size	25	nm
Domain size	2.5 x 2.5 x 2.5	μm
Volumetric concentration of kerogen	20	%
Total porosity	5	%
Water saturation	100	%
Formation temperature	175	°F
Resistivity of grains	10^7	ohm-m
Resistivity of connate water at 175 °F	0.05	ohm-m
Resistivity of kerogen at 175 °F	1 - 10^7	ohm-m

Next, two synthetic 3D images of organic-rich source rock were developed with similar volumetric concentration of kerogen, water saturation, and porosity but different spatial connectivity of kerogen and water phase (**Figure 19**). The network shown in **Figure 19a** had less kerogen-water-network connectivity compared to the one shown in **Figure 19b**. The petrophysical, compositional, and electrical parameters assumed in the numerical

simulations were similar to those reported in **Table 2**. The electrical resistivity of kerogen was assumed as 100 ohm-m in both cases.

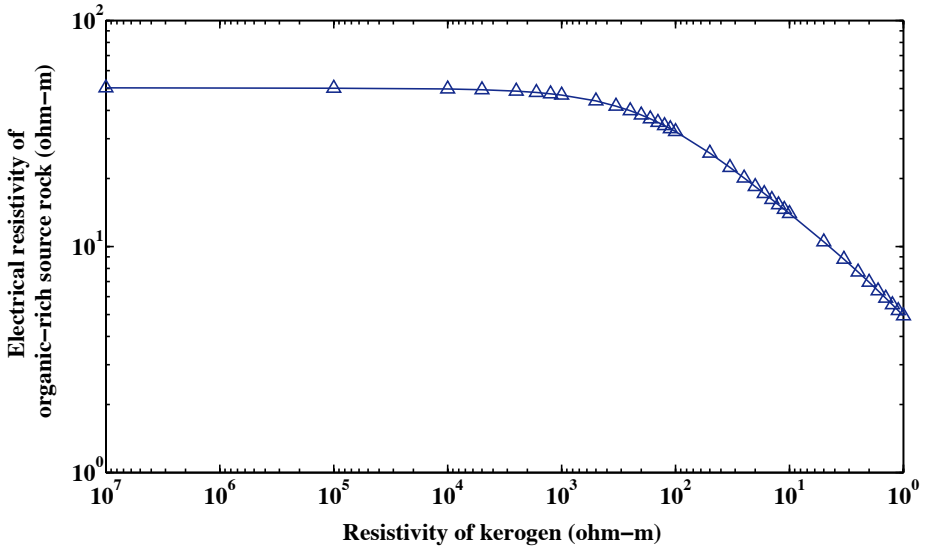

Figure 18: Synthetic Case No. 2: Impact of kerogen conductivity on electrical resistivity of three-dimensional pore-scale image of organic-rich source rock.

The calculated electrical resistivity for the less connected kerogen-water network was 22.63 ohm-m while that of the more connected kerogen-water network was 13.83 ohm-m. This difference corresponds to a 39% relative decrease in electrical resistivity due to an increase in kerogen-water-network connectivity. The decrease in effective rock electrical resistivity has a significant impact on the estimates of fluid saturation using conventional resistivity-porosity-saturation models, which leads to a 30% overestimate in water saturation, in this case.

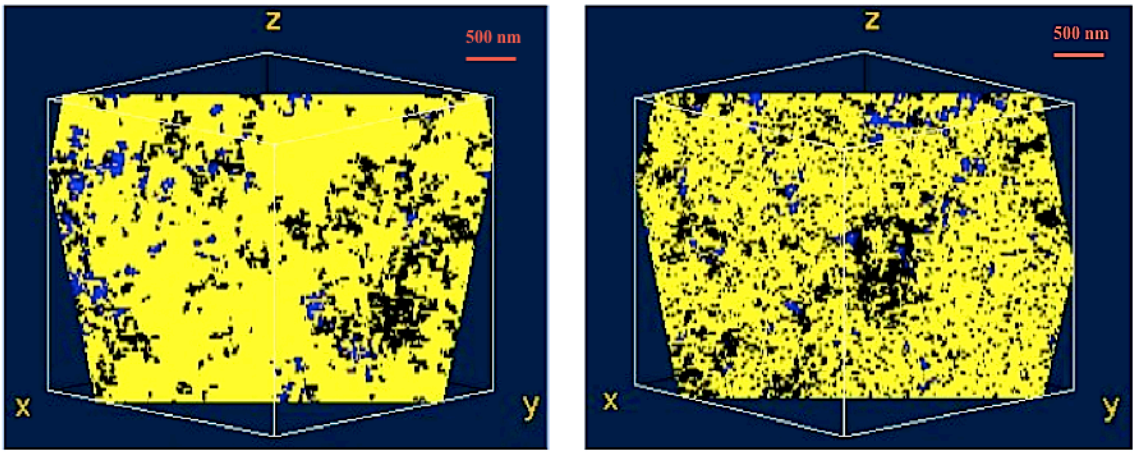

Figure 19: Synthetic Case No. 2: Three-dimensional pore-scale images of two organic-rich source rocks with (a) low connectivity and (b) high connectivity of kerogen-water network. Yellow, blue, and black areas in the 3D image represent grains, water, and kerogen, respectively.

4.3 Synthetic Case No. 3: Effective electrical resistivity of gas-saturated kerogen

Presence of gas in nano-scale pore structure within kerogen is another parameter affecting electrical resistivity of organic-rich source rocks. Previous publications suggested about 50% of the volume of the organic matter in overmature organic-rich source rocks may consist of hydrocarbon-wet pores (Passey et al., 2010). A recently introduced petrophysical model for organic-rich source rocks assumes that hydrocarbon phase occupies the kerogen pore space while matrix porosity is filled with water (Alfred et al., 2012). Synthetic Case No. 3 investigates the impact of gas-filled pore space inside kerogen on the effective electrical resistivity of kerogen-gas system.

First, 3D synthetic images of kerogen-gas system were developed by randomly distributing gas-filled pores within the kerogen domain. Three kerogen-gas systems were built with kerogen electrical resistivity of 1000 ohm-m, 500 ohm-m, and 100 ohm-m. Gas-filled pores were assumed to have a size of 25nm by 25nm by 25nm. Gas in the pores was assumed to be non-conductive with an electrical resistivity of 10^7 ohm-m. Effective electrical resistivity of gas-filled kerogen was then estimated using the developed numerical simulator. A progressive increase in the gas-filled kerogen porosity (i.e., from 5% - 50%) quantified the impact of gas-filled pores on effective electrical resistivity of kerogen-gas system. The estimated electrical resistivity was the median of results from 20 random distributions of fully gas-saturated kerogen pores for each case of gas-filled kerogen porosity.

Figure 20 illustrates the correlation between gas-filled kerogen porosity and electrical conductivity of kerogen. Based on the sensitivity analysis, an empirical correlation between gas-filled kerogen porosity and effective electrical resistivity of kerogen-gas system is given by

$$R_{effK} = 0.924 R_k e^{1.78\phi_k} \quad , \tag{28}$$

where R_{effK} is the effective electrical resistivity of kerogen-gas system, R_k is the electrical resistivity of kerogen, and ϕ_k is the gas-filled kerogen porosity.

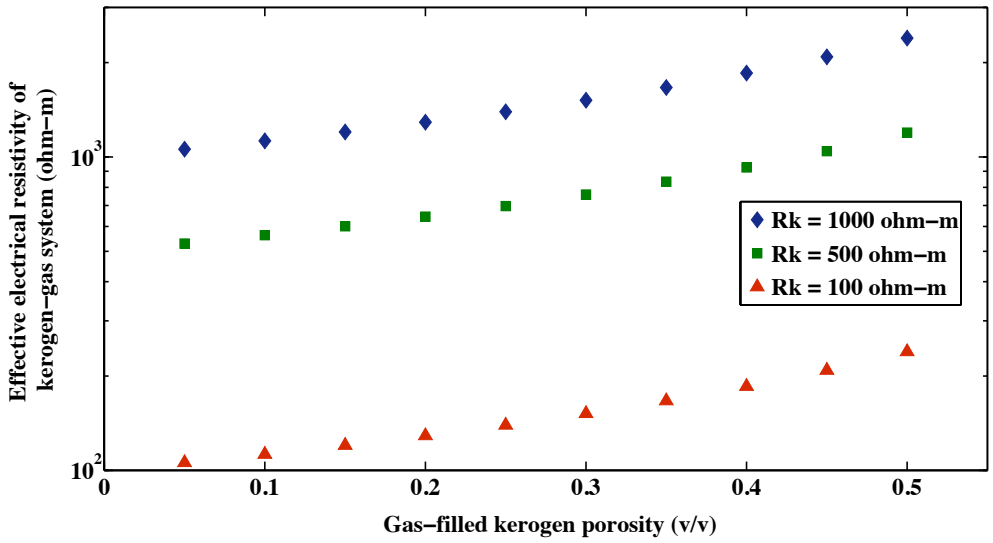

Figure 20: Synthetic Case No. 3: Correlation between the effective electrical resistivity of kerogen-gas system and gas-filled kerogen porosity. Blue, red, and green points show the effective electrical resistivity of kerogen-gas system when electrical resistivity of kerogen is assumed to be 1000 ohm-m, 500 ohm-m, and 100 ohm-m, respectively.

In the next synthetic case study, numerical simulations were performed on 3D organic-rich source rocks with gas-saturated kerogen. The effect of conductive gas-saturated kerogen on electrical resistivity measurements in organic-rich source rocks and its impact on estimates of hydrocarbon saturation using conventional resistivity-porosity-saturation models is discussed.

4.4 Synthetic Case No. 4: Organic-rich source rocks with gas-saturated kerogen

Synthetic Case No. 4 examines the effect of conductive gas-saturated kerogen on electrical resistivity of organic-rich source rocks. 3D images of organic-rich source rock

were developed with the pore structure and spatial distribution of kerogen similar to Synthetic Case No. 3. In this case, matrix pores were fully saturated with brine and kerogen pores were fully saturated with gas. The electrical conductivity of kerogen was varied to investigate its impact on effective electrical resistivity of 3D organic-rich source rock. Kerogen porosity, however, remained constant.

First, the effective electrical resistivity of the synthetic organic-rich source rock was estimated for different electrical conductivities of kerogen using numerical simulations. **Table 3** lists the assumed petrophysical, electrical, and modeling parameters for Synthetic Case No. 4. Next, the estimated effective electrical resistivity of the rock was used to calculate the water saturation using a conventional resistivity-porosity-saturation model (i.e., Archie's equation in this case).

Figure 21 shows the relative difference between the estimated water saturation using Archie's equation in the presence of conductive kerogen and the estimated water saturation assuming kerogen is non-conductive. For instance, in the presence of conductive kerogen with 100 ohm-m resistivity, Archie's equation overestimated water saturation by 23%. Taking into account the effect of conductive kerogen on electrical resistivity of organic-rich source rocks can improve estimates of hydrocarbon saturation by 10% - 23%.

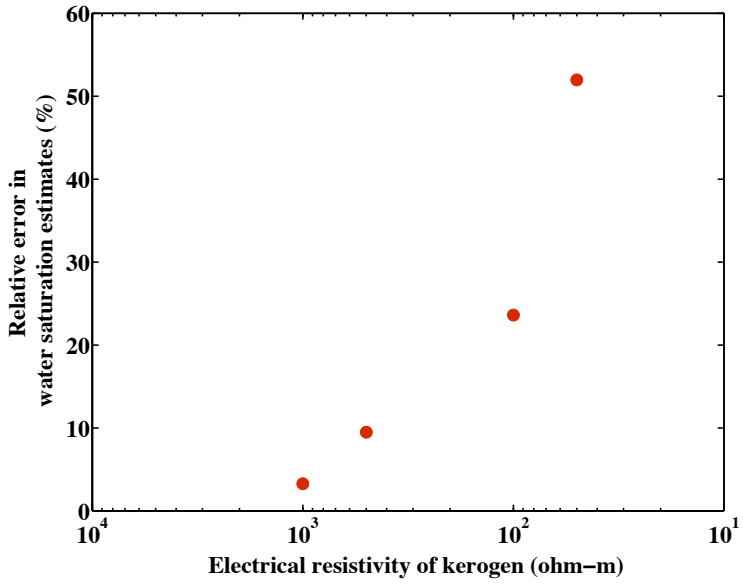

Figure 21: Synthetic Case No. 4: Impact of electrical resistivity of kerogen on relative error in estimates of water saturation if obtained using conventional resistivity-porosity-saturation models (i.e., Archie's equation in this case).

The relative error in estimates of water saturation due to the presence of conductive kerogen depends on the salt concentration of connate water present in the organic-rich source rock. If the salt concentration of connate water is high, then the relative impact of conductive kerogen on effective electrical resistivity of organic-rich source rock is small. A sensitivity analysis was performed on the impact of salt concentration of connate water (varied from 60 kppm NaCl to 200 kppm NaCl) on relative error in water saturation estimates if obtained using conventional-resistivity-saturation models in the presence of conductive kerogen with 100 ohm-m resistivity. **Figure 22** illustrates the decreasing impact of conductive kerogen on the relative error in water saturation estimates when salt concentration of connate water increases.

Table 3: Synthetic Case No. 4: Summary of the assumed petrophysical, electrical, and modeling parameters.

Variable	**Value**	**Units**
Grid size	25	nm
Domain size	2.5 x 2.5 x 2.5	μm
Matrix porosity	5	%
Volumetric concentration of kerogen	20	%
Gas-filled kerogen porosity	35	%
Formation temperature	175	°F
Resistivity of grains	10^7	ohm-m
Resistivity of connate water at 175 °F	0.05	ohm-m
Resistivity of gas	10^7	ohm-m
Resistivity of kerogen at 175 °F	1 - 10^7	ohm-m
Archie's factor, *a*	1	[ ]
Archie's porosity exponent, *m*	2.18	[ ]
Archie's saturation exponent, *n*	2.12	[ ]

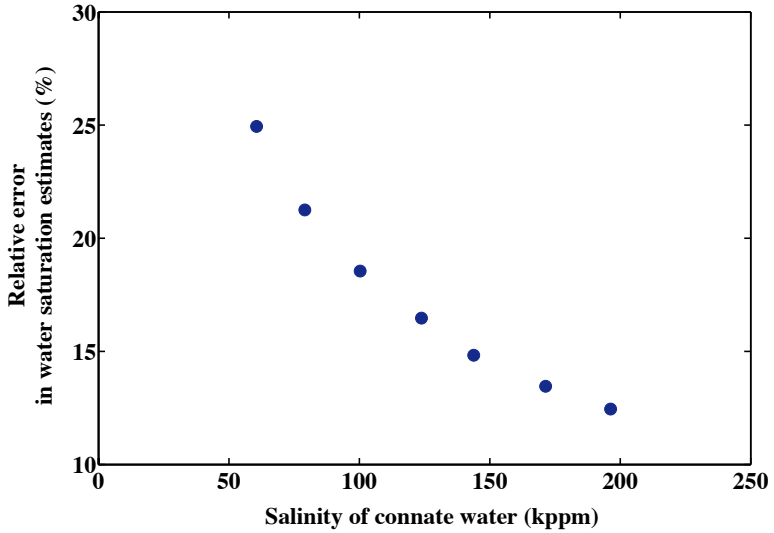

Figure 22: Synthetic Case No. 4: Impact of salt concentration of connate water on the relative error in water saturation estimates due to the presence of conductive kerogen with 100 ohm-m resistivity.

Furthermore, the impact of kerogen porosity on effective electrical resistivity of organic-rich source rocks was examined. Sensitivity analysis was performed by progressively increasing kerogen porosity, while all other petrophysical and compositional parameters were assumed constant. **Figure 23** shows the effect of kerogen porosity on the effective electrical resistivity of the rock in the presence of conductive kerogen with 100 ohm-m resistivity. The effective electrical resistivity of the organic-rich rock-fluid system increases, when gas-filled kerogen porosity increases.

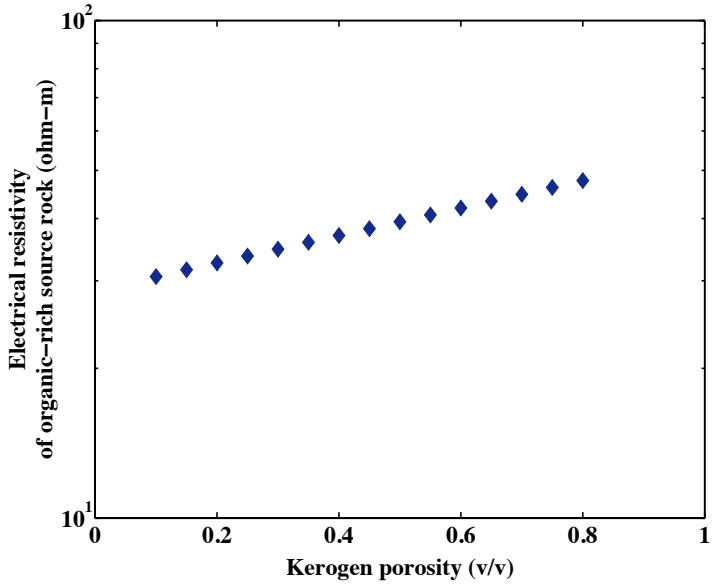

Figure 23: Synthetic Case No. 4: Impact of kerogen porosity on effective electrical resistivity of organic-rich source rocks.

CHAPTER V

CONCLUSIONS

This chapter summarizes the main contributions of the work described in this thesis, provides conclusions drawn from the results of well-log interpretation and pore-scale numerical simulations, and suggests recommendations for future work.

5.1 Summary

The objective of this thesis was to investigate and quantify the effect of petrophysical and compositional properties of organic-rich source rocks on electrical resistivity measurements in these formations. First, joint interpretation of well logs and core measurements from a field example in the Haynesville shale-gas formation was performed to examine the reliability of conventional resistivity-porosity-saturation models in assessment of water saturation in organic-rich source rocks. Next, a pore-scale numerical simulator was developed using finite difference method to discretize the Laplace conductivity equation in porous media. The numerical simulator solves for spatial distribution of electric field potential, electric current and estimates effective electrical resistivity of pore-scale rock-fluid systems. The numerical simulations were performed using a single compute node on the supercomputer. Each node had 24 GB of DDR3 1333 MHz memory with each core operating at 2.8 GHz. CPU time for 2D numerical simulations discussed in Synthetic Case No. 1 was 4 hours. This increased to

around 24 hours - 72 hours for 3D numerical simulations, in highly heterogeneous porous media, reported in Synthetic Cases 2, 3, and 4. Further, sensitivity analysis was performed using the numerical simulator to investigate the impact of volumetric concentration of kerogen, electrical conductivity of kerogen, spatial distribution of kerogen, connectivity of kerogen-water network, and kerogen porosity on electrical resistivity of organic-rich source rocks.

5.2 Conclusions

The main conclusions drawn from this thesis can be summarized as follows:

- Well-log interpretation in the Haynesville shale-gas formation showed that conventional resistivity-porosity-saturation models were not reliable for assessment of hydrocarbon saturation using electrical resistivity measurements.
- Relative errors ranging from 20% - 40% in estimates of water saturation from conventional models compared to core measurements were observed in the zones with high volumetric concentration of kerogen. This could be due to highly mature conductive kerogen and/or presence of conductive mineral such as pyrite inside the kerogen network.
- Results from numerical simulations performed in Synthetic Case No. 1 illustrated the impact of kerogen conductivity, and volumetric concentration of kerogen on electrical resistivity of pore-scale images with layered and dispersed spatial distributions of kerogen. The effective electrical resistivity of organic-rich source

rocks decreased for both layered and dispersed kerogen when the electrical conductivity of kerogen and volumetric concentration of kerogen increased. However, a steeper decline was observed in layered spatial distribution of kerogen compared to that of dispersed spatial distribution of kerogen. This difference is attributed to the increased directional connectivity of kerogen network in the layered case compared to the dispersed case.

- Results from Synthetic Case No. 2 illustrated the effect of spatial distribution and connectivity of kerogen-water phase on electrical resistivity of organic-rich source rock. The increased connectivity in 3D pore-scale representations of organic-rich source rock had a significant impact on effective electrical resistivity of the rock-fluid system. The effect of kerogen on effective electrical resistivity of organic-rich source rock was observed at kerogen electrical resistivities less than 1000 ohm-m (compared to 100 ohm-m in the case of 2D images of organic-rich source rocks). Furthermore, it was observed that the electrical resistivity of organic-rich source rocks decreased by 39% if connectivity of kerogen-water network increased, while kerogen concentration remained the same.
- Results from Synthetic Case No. 3 provided an empirical correlation between the gas-filled kerogen porosity and effective electrical resistivity of kerogen-gas system. This correlation can be used to estimate the effective electrical resistivity of the kerogen-gas system at different thermal maturities.

- Synthetic Case No. 4 illustrated the significant impact of conductive kerogen on effective electrical resistivity of organic-rich source rocks with gas-saturated kerogen. Results from pore-scale numerical simulations showed a 10% - 23% improvement in accuracy of water saturation estimates when the impact of conductive kerogen was taken into account.
- The results reported in this thesis can be used to develop a new resistivity-porosity-saturation model, which takes into account the presence of highly mature conductive kerogen. This would significantly improve estimates of hydrocarbon saturation as part of the combined petrophysical interpretation of well logs in organic-rich source rocks.

5.3 Recommendations

The following provides recommendations for future work to expand on the work reported in this thesis:

- The electrical resistivity of kerogen assumed in this thesis is 2-3 orders of magnitude higher than the conductivities observed in pure organic semi-conductors at reservoir temperature. However, accurate electrical resistivity values for kerogen are required, which need to be obtained using laboratory experiments.
- Finite difference based numerical simulator developed in this thesis was restricted in terms of the grid size that can be used. Performing numerical

simulations become computationally expensive for grid numbers greater than 300x300x300. Application of parallel computing would help improve CPU time and increase computational efficiency.

- Numerical simulations using finite difference methods in highly heterogeneous porous media can be computationally expensive due to increased grid numbers. Application of finite element methods or streamline-based numerical simulation methods can decrease computational time compared to finite difference methods.
- This thesis studied the effect of kerogen conductivity, volumetric concentration of kerogen, spatial distribution and connectivity of kerogen-water network, and kerogen porosity on electrical resistivity measurements in organic-rich source rocks. This research could be extended to study the impact of spatial distribution and connectivity of pyrite, relative conductivity of clay to that of formation water, and spatial connectivity of kerogen on electrical resistivity measurements. It would then be possible to develop a new resistivity-porosity-saturation model that takes into account the petrophysical, compositional, and electrical properties of organic-rich source rocks.

REFERENCES

Alfred, D. and Vernik, L., 2012, A new petrophysical model for organic shales: *Transactions of the SPWLA 53rd Annual Logging Symposium*, Cartagena, Columbia, June 16-20.

Barwise, A. J. G., Mann, A. L., Eglinton, G., Gowar, A. P., Wardroper, A. M. K., and Gutteridge, C. S., 1984, Kerogen characterization by 13C NMR spectroscopy and pyrolysis-mass spectrometry: *Organic Geochemistry*, vol. 6, p. 343–349.

Dennis, L. W., Maciel, G. E., Hatcher, P. G., and Simoneit, B. R. T., 1982, 13C Nuclear magnetic resonance studies of kerogen from Cretaceous black shales thermally altered by basaltic intrusions and laboratory simulations: *Geochimica et Cosmochimica Acta*, vol. 46, p. 901–907.

Hammes, U., Eastwood, R., Rowe, H. D., and Reed, R. M., 2009, Addressing conventional parameters in unconventional shale-gas systems: depositional environment, petrography, geochemistry, and petrophysics of the Haynesville Shale, *Unconventional energy resources: making the unconventional conventional: 29th Annual GCSSEPM Foundation Bob F. Perkins Research Conference*, p. 181–202, Houston, December 6–8.

Heidari, Z., Torres-Verdin, C., and Pregg, W. E., 2012, Improved estimation of mineral and fluid volumetric concentrations from well logs in thinly bedded and invaded formations: *Geophysics*, vol. 77, no. 3, p. 79-98.

Heidari, Z., Torres-Verdin, C., and Pregg, W. E., 2011, Quantitative method for estimating total organic carbon and porosity, and for diagnosing mineral constituents from well logs in shale-gas formations: *Transactions of the SPWLA 52nd Annual Logging Symposium*, Colorado Springs, Colorado, May 14-18.

Li, L., Meller, G., and Kosina, H., 2007, Temperature and field-dependence of hopping conduction in organic semiconductors: *Microelectronics Journal*, vol. 38, p. 47-51.

Mao, J., Fang, X., Lan, Y., Schimmelmann, A., Mastalerz, M., Xu, L., and Schmidt-Rohr, K., 2010, Chemical and nanometer-scale structure of kerogen and its change during thermal maturation investigated by advanced solid-state ^{13}C NMR spectroscopy: *Geochimica et Cosmochimica Acta*, vol. 74, p. 2110-2127.

Meng, D., Ma, T. M., Geng, C. W., and Sun, Y., 2012, Test method and experimental research on resistance of oil shale under high temperature: *Global Geology*, vol. 15(3), p. 245-251.

Miknis, F. P., Smith, J. W., Maughan, E. K., and Maciel, G. E., 1982, Nuclear magnetic resonance: a technique for direct nondestructive evaluation of source-rock potential: *AAPG Bulletin-American Association of Petroleum Geologists*, vol. 66, p. 1396–1401.

Miknis, F. P., Jiao, Z. S., Macgowan, D. B., and Surdam, R. C., 1993, Solid-state NMR characterization of Mowry shale from the Powder River Basin: *Organic Geochemistry*, vol. 20, p. 339–347.

Passey, Q. R., Creaney, S., Kulla, J. B., Moretti, F. J., and Stroud, J. D., 1990, A practical model for organic richness from porosity and resistivity logs: *The American Association of Petroleum Geologists*, vol. 74, no. 12, p. 1777-1794.

Passey, Q. R., Bohacs, K. M., Esch, W. L., Klimentidis, R., and Sinha, S., 2010, From oil-prone source rock to gas-producing shale reservoir – geologic and petrophysical characterization of unconventional shale-gas reservoirs: Paper SPE 131350*, Proceedings of the CPS/SPE International Oil and Gas Conference and Exhibition*, Beijing, China, 8–10 June.

Patience, R. L., Mann, A. L., and Poplett, I. J. F., 1992, Determination of molecular

structure of kerogens using 13C NMR spectroscopy: II. The effects of thermal maturation on kerogens from marine sediments: *Geochimica et Cosmochimica Acta,* vol. 56, p. 2725–2742.

Quirein, J., Witkowsky, J., Truax, J., Galford, J., Spain, D., and Odumosu, T. 2010, Integrating core data and wireline geochemical data for formation evaluation and characterization of shale gas reservoirs: Paper SPE 134559, *Proceedings of the SPE Annual Technical Conference and Exhibition*, Florence, Italy, 19-22 September.

Rajeshwar, K., Das, M., and Dubow, J., 1980, D.C. electrical conductivity of Green River oil shales: *Nature*, vol. 287, p. 131-133.

Ramirez, T. R., Klein, J. D., Bonnie, R. J. M., and Howard, J. J., 2011, Comparative study of formation evaluation methods for unconventional shale-gas reservoirs: application to the Haynesville Shale (Texas): Paper SPE 144062, *Proceedings of the SPE North American Unconventional Gas Conference and Exhibition*, The Woodlands, Texas, USA, 14-16 June.

Requejo, A. G., Gray, N. R., Freund, H., Thomann, H., Melchior, M. T., Gebhard, L. A., Bernardo, M., Pictroski, C. F., and Hsu, C. S., 1992, Maturation of petroleum source

rocks. 1. Changes in kerogen structure and composition associated with hydrocarbon generation: *Energy & Fuels*, vol. 6, p. 203–214.

Smernik, R. J., Schwark, L., and Schmidt, M. W. I., 2006, Assessing the quantitative reliability of solid-state C-13 NMR spectra of kerogens across a gradient of thermal maturity: *Solid State Nuclear Magnetic Resonance*, vol. 29, p. 312–321.

Solli, H., Van Graas, G., Leplat, P., and Krane, J., 1984, Analysis of kerogens of miocene shales in a homogenous sedimentary column. A study of maturation using flash pyrolysis techniques and carbon-13 CP-MAS NMR: *Organic Geochemistry*, vol. 6, p. 351–358.

Sondergeld, C. H., Newsham, K. K., Comisky, J. T., Rice, M. C., and Rai, C. S., 2010, Petrophysical considerations in evaluating and producing shale gas resources: Paper SPE 131768, *Proceedings of the SPE Unconventional Gas Conference*, Pittsburg, Pennsylvania, USA, 23-25 February.

Wei, Z. B., Gao, X. X., Zhang, D. J., and Da, J., 2005, Assessment of thermal evolution of kerogen geopolymers with their structural parameters measured by solid-state C-13 NMR spectroscopy: *Energy & Fuels*, vol. 19, p. 240–250.

Werner-Zwanziger, U., Lis, G., Mastalerz, M., and Schimmelmann, A., 2005, Thermal maturity of type II kerogen from the New Albany Shale assessed by C-13 CP/MAS NMR: *Solid State Nuclear Magnetic Resonance*, vol. 27, p. 140–148.

Witte, E. G., Schenk, H. J., Muller, P. J., and Schwochau, K., 1988, Structural modifications of kerogen during natural evolution as derived from 13C CP/MAS NMR, IR spectroscopy and Rock-Eval pyrolysis of Toarcian shales: *Organic Geochemistry*, vol. 13, p. 1039–1044.